MICROFLUIDIC NETWORKING: MODELLING AND ANALYSIS

RELATORE: Ch.mo Prof. Andrea Zanella

LAUREANDO: Andrea Biral

A.A. 2012-2013

UNIVERSITÀ DEGLI STUDI DI PADOVA
DIPARTIMENTO DI INGEGNERIA DELL'INFORMAZIONE
TESI DI LAUREA MAGISTRALE IN INGEGNERIA DELLE
TELECOMUNICAZIONI

MICROFLUIDIC NETWORKING: MODELLING AND ANALYSIS

RELATORE: Ch.mo Prof. Andrea Zanella

LAUREANDO: Andrea Biral

Padova, 10 dicembre 2012

Abstract

Droplets microfluidics refers to manipulation and control of little amounts of fluids flowing into channels of micro-scale size. Our aim, pursued in the present thesis, is to design a network formed by such microchannels and define a model to properly route the droplets inside them. However, this kind of study relies on the preliminary deep knowledge of microfluidic flow dynamics and typical propagation characteristics. Accordingly, we begin our dissertation by introducing the physical laws that govern microfluidics. Then, we discuss the current understandings about droplets formation, transport and their behavior in bifurcating channels, corroborating all with simulative results. Furthermore, we show how such concepts can be integrated in our networking solution and, lastly, we implement a microfluidic network with bus topology and illustrate its performance.

Contents

Chapter 1

Introduction

Microfluidic is both a science and a technology that deals with the control of small amounts of fluids flowing through microchannels. These have dimension in the order of micrometers and are usually fabricated in PDMS, i.e., *Polydimethylsiloxane*, which is a silicon based organic polymer. In this thesis we are specifically interested in droplets microfluidics which is a science related to the control of the motion dynamics of droplets in such microchannels. In this scenario, small drops are dispersed into another fluid, which is immiscible with them; this is why in literature they are conventionally called *dispersed phase*, while the immiscible substance in which they are immersed is called *continuous phase*.

This line of reserch has emerged strongly in the past few years but the field is still at an early stage of development. Nevertheless its capabilities and advantages are already well known. The so called droplet microfluidics technology, in fact, exploits both its most obvious characteristic (small size) and less obvious characteristics of fluid in microchannels (such as laminar flow) to provide new capabilities in the control and concentrations of molecules in space and time. Moreover it has the potential to influence many subject areas from chemical synthesis and biological analysis to optics and information technology.

Nowadays, applications of microfluidics span from inkjet printheads to DNA chips, from micro-propulsion to micro-thermal technologies. However, the most promising utilization of microfluidic technologies have just been in analysis, for which they offer a number of useful capabilities: the ability to use very small quantity of samples and reagents and to carry out separations and detections with high resolution and sensitivity, low cost, short time for analysis and small

footprint for the analytical devices. All these advantages however come at the price of raise a new set of fluid dynamical problems that appear due to the deformable interface of the droplets, the need to take into account interfacial tension and its variations, and the complexity of singular events such as splitting drops. In the physicist's vocabulary, droplets introduce nonlinear laws into the otherwise linear Stokes flows. Evidence of this nonlinearity can be found, for instance, by considering that different flow regimes can appear in the same channel and under similar forcing conditions. These transitions between widely different behaviors are possible because modifications in the drop geometry couple back to the flow profiles and amplify initially small variations. A large body of work has recently attempted to tackle these fluid dynamical questions, leading along the way to creative new design for microfluidic devices -e.g., *Labs-on-a-Chip* (see Figure 1.1)- and new physical approaches to control the behavior of drops.
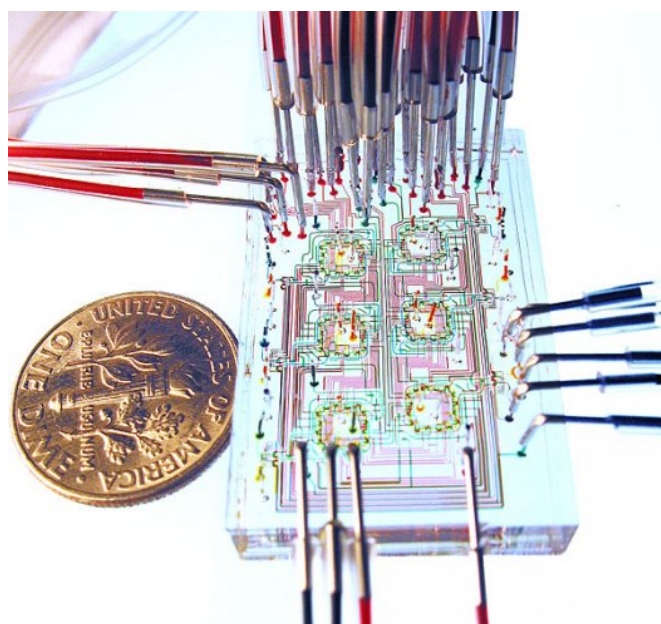
Figure 1.1: Example of *Lab-on-a-chip*: a microfluidic chemostat used to study the growth of microbial populations.

In the future, one may envision microfluidic systems with mazes of microchannels along which droplets conveying solutes, materials and particles undergo transformations and reactions. These devices could be used to perform all sort of bio-/physiochemical analysis or to produce novel entities by means of specific "microfluidic machines" able to process fluids at such a scale. This particular scenario

has inspired the following work. Indeed, our idea is to create a network, consisting of microchannels, in order to connect with each other more microfluidic machines. In this way, we could miniaturize and automate in a single device an entire laboratory gaining, at the same time, in versatility and flexibility. In fact, once a specific microfluidic machine has opportunely processed an incoming droplet, the latter might be reinjected in the network to reach another target microfluidic machine undergoing further transformations and so on. Moreover, we could parallelize the tasks undertaken by different microfluidic machines obtaining a consequent, significant time saving. Such a prospective requires, however, preliminarily, the control over elementary operations like droplet production, breakup, transport and redirection. This motivated us to structure the present thesis as described below.

In *Chapter 2* we introduce the main underlying concepts of droplets microfluidics in order to let the reader familiarize with the notation and the physical ingredients typical of this science.

Chapter 3, instead, is dedicated to the study of droplet production in microchannels. In particular, it contains a brief review of the three main approaches proposed, in this regard, in literature with a particular focus on the solution that satisfy our requirements the most. Furthermore, here we also present a set of simulative results obtained with the CFD software OpenFOAM (see Appendix A) in order to validate the theoretical basis introduced.

In the first half of *Chapter 4* we treat the dynamics of droplet breakup in a junction. The latter is, of course, a founding part of our microfluidic network since it is an indispensable element to direct the droplets to the various target microfluidic machines. This topic is very important to us because we need to preserve the integrity of the droplets throughout the entire network and, thus, even when they face "sensitive points" like bifurcations. Therefore, here, we'll analyze in details the conditions that allow us to transport droplets avoiding their splitting in the channels' ramifications.

Then, in the second part of the chapter, we present a model for the programmable partitioning of droplets at a T-junction illustrating how we can direct

them in the desired branch of the bifurcation. Once again, we corroborate our conclusions with corresponding numerical simulations obtained at the calculator.

In *Chapter 5* we finally introduce a microfluidic bus-shaped network, discuss the mathematical and physical constraints that we need to respect in order to correctly dimension it and then illustrate the performance of such a system.

Lastly, *Chapter 6* focuses on the possible future developments of the thesis, anticipating eventual improvements and alternative solutions.

Chapter 2

Basic microfluidic concepts

The present chapter is intended to give an overview of the microfluidic's physical basis by collecting and describing the main parameters and models which rule fluid transport and droplet dynamics in microfluidic systems. Thus, the aim of this section is to allow the reader to familiarize with the principal concepts of microfluidic that will be recalled and further analyzed throughout the entire work.

2.1 Viscosity

Viscosity is a measure of the resistance of a fluid which is being deformed by either shear stress or tensile stress. In simple terms, it describes a fluid's internal resistance to flow and may be thought of as a measure of fluid friction: the greater the viscosity, the greater its resistance to flow and vice versa. With the exception of superfluids, all real fluids have some resistance to stress and therefore are viscous. In common usage, a liquid with a viscosity less than water is known as mobile liquid while, in the opposite case, it is called viscous liquid. Synthetically, the physical behavior associated with viscosity can be described as follows: in any flow, molecule's layers move at different velocities and the fluid's viscosity arises from the shear stress between the layers that ultimately opposes any applied force. The relationship between the shear stress and the velocity gradient can be obtained by considering two plates closely spaced at a distance y, and separated by a homogeneous substance. Assuming that the plates are very large, with a large area A, such that edge effects may be ignored, and that the lower plate

is fixed, let a force F be applied to the upper plate. If this force causes the substance between the plates to undergo shear flow with a velocity gradient u/y, it results:

$$F = \mu A \frac{u}{y}, \tag{2.1}$$

where $\mu [Pa \cdot s]$ is the proportionality factor called dynamic viscosity. It should be noted that viscosity is a function of temperature: fluid become less viscous as temperature increases. In this thesis, however, we assume the temperature is constant during the operation of microfluidic devices. Water at 20℃ has a characteristic dynamic viscosity of $1.002 \cdot 10^{-3} Pa \cdot s$.

Equation (2.1) can also be expressed in terms of shear stress ($\tau = \frac{F}{A}$). In particular, as reported in differential form by Isaac Newton for straight, parallel and uniform flow, the shear stress between layers is proportional to the velocity gradient in the direction perpendicular to the layers: $\tau = \mu \frac{\partial u}{\partial y}$. Newton's law of viscosity, given above, is a constitutive equation which holds for the so called Newtonian fluids. Non-Newtonian fluids, instead, exhibit a more complicated relationship between shear stress and velocity gradient than simple linearity. The analysis of the latter, however, is beyond the scope of this work since we will be dealing only with Newtonian fluid.

Finally, in many situations we are concerned with the ratio between the dynamic viscosity and the density of the fluid: $\nu = \frac{\mu}{\rho}$ which is a coefficient named kinematic viscosity. The SI physical unit of ν is $[m^2/s]$. Water at 20℃ has a characteristic dynamic viscosity of about $10^{-6} m^2/s$.

2.2   Capillary number

In fluid dynamics, the Capillary number represents the relative magnitude of viscous forces versus surface tension acting across an interface between a liquid and a gas, or between two immiscible liquids. It is a dimensionless parameter defined as:

$$Ca = \frac{\mu u}{\sigma} \tag{2.2}$$

where $\mu [Pa \cdot s]$ is the viscosity of the main liquid, $u[m/s]$ is its mean velocity and $\sigma [N/m]$ is the surface or interfacial tension coefficient between the two fluid phases.

With reference to the droplet microfluidic context:

$$Ca = \frac{\mu_c u_c}{\sigma} \tag{2.3}$$

where $\mu_c[Pa{\cdot}s]$ is the viscosity of the carrier fluid in which droplets are immersed, $u_c[m/s]$ is its mean velocity and $\sigma[N/m]$ is the interfacial tension coefficient between continuous and dispersed phase.

Since viscous stress represents a destructive force while interfacial tension acts as a cohesive force, Capillary number may be thought of as a measure of the cohesion of the droplet: the greater is the Capillary number, the greater the probability of droplet splitting and vice versa.

2.3   Reynolds number

In fluid dynamics the Reynolds number is a dimensionless parameter that gives a measure of the ratio of inertial forces to viscous forces and consequently quantifies the relative importance of these two types of forces for given flow conditions.

Reynolds numbers frequently arise when performing dimensional analysis of fluid dynamics problems, and as such can be used to determine dynamic similitude between different experimental cases. They are also used to characterize different flow regimes, such as laminar or turbulent flow: laminar flow (see Section §2.4) occurs at low Reynolds numbers, where viscous forces are dominant, and is characterized by smooth, constant fluid motion; turbulent flow occurs at high Reynolds numbers and is dominated by inertial forces, which tend to produce chaotic eddies, vortices and other flow instabilities.

Mathematically, Reynolds number is defined as follows:

$$Re = \frac{\rho u L}{\mu} \tag{2.4}$$

where $\mu[Pa{\cdot}s]$ is the viscosity of the liquid, $u[m/s]$ is its mean velocity, $\rho[kg/m^3]$ is its density and $L[m]$ is a characteristic linear dimension of the system. Declining it in the microfluidic context, L is conventionally considered equal to the hydraulic diameter of the channel ($D_H = 4A/P$, where A is the cross sectional area of the channel and P is the wetted perimeter of the channel), μ is the viscosity of the carrier liquid (μ_c), u is its mean velocity (u_c) and ρ is its density (ρ_c). Thus:

$$Re = \frac{4A\rho_c u_c}{P\mu_c} \tag{2.5}$$

2.4   Laminar flow

In fluid dynamics, laminar flow, sometimes known as streamline flow, is a flow regime characterized by high momentum diffusion and low momentum convection that involves a very orderly motion of fluid's particles which are organized in parallel layers (or laminae). Although all the molecules move in straight lines, they are not all uniform in velocity: if the mean velocity of the flow is u, then the molecules at the centre of the tube are moving at approximately $2u$, whilst the molecules at the side of the tube are almost stationary. Moreover, in this regime, the fluid tends to flow without lateral mixing, there are no cross currents perpendicular to the direction of flow, nor eddies or swirls of fluids.

This kind of behavior occurs as long as the Reynolds number (see Section §2.3) is below a specific critical value $Re_{CR} \simeq 2000$ that depends on the particular flow geometry and can be sensitive to disturbance levels and imperfections present in a given configuration. Bearing in mind this condition, laminar flow is exactly the regime we would expect to see in typical microfluidic systems since their characteristic small length-scales ($L \simeq 10^{-6}m$) and slow fluid velocities ($u \simeq 10^{-3}m/s$) lead to very low Reynolds number ($Re = \frac{\rho u L}{\mu} \simeq 10^{-3}$).

Further, when Reynolds number is much less than 1, which is the case of our competence, creeping motion (or Stokes flow) occurs. This is an extreme case of laminar flow where viscous (friction) effects are much greater than inertial forces. This physical phenomenon entails two additional interesting properties in incompressible Newtoninan fluids:

- Instantaneity: a Stokes flow has no dependence on time other than through time-dependent boundary conditions. This means that, given the boundary conditions of a Stokes flow, the flow can be found without knowledge of the flow at any other time;

- Time-reversibility: a time-reversed Stokes flow solves the same equations as the original Stokes flow. Practically, it implies that it is difficult to mix two fluids using creeping flow.

2.5 Hagen-Poiseuille's law

In fluid dynamics, the Hagen-Poiseuille equation is a physical law that relates the pressure drop in a fluid flowing through a long pipe with its volumetric flow rate. The assumptions of the equation are that the fluid is viscous and incompressible, the flow is laminar through a channel of constant cross-section and there is no acceleration of fluid. These hypotheses, as we already pointed out, are fully satisfied in the typical microfluidic systems.

Now, in order to derive Hagen-Poiseuille's law, let's begin considering the incompressible Navier-Stokes equation for uniform-viscous Newtonian fluids with no body forces:

$$\rho \frac{\partial \vec{u}}{\partial t} = -\rho \vec{u} \nabla \vec{u} - \nabla p + \mu \nabla^2 \vec{u} \tag{2.6}$$

where $\vec{u}\,[m/s]$ is the velocity field, which is the description of the velocity of the fluid at a given point in space and time, and is denoted by $\vec{u} = \vec{u}(\vec{r}, t)$, where $\vec{r}\,[m]$ is a position vector specifying a location in space and $t\,[s]$ is time; $\rho\,[kg/m^3]$ is the fluid density; $\mu\,[Pa \cdot s]$ is the dynamic viscosity and $p\,[Pa]$ is the pressure. More specifically, in Equation (2.6), $\rho \frac{\partial \vec{u}}{\partial t}$ represents the rate of change of momentum, $-\rho \vec{u} \nabla \vec{u}$ concerns convective force, $-\nabla p$ describes the pressure force while viscous force is indicated in the term $\mu \nabla^2 \vec{u}$.

Let's then consider a long cylindrical channel with the x-direction along the axis of the channel. In the steady-state of fully developed fluid flow in the channel, its velocity field is unidirectional and laminar and there is no acceleration of the fluid. Thus, the unsteady and convection terms are all zero, and Equation (2.6) becomes:

$$\nabla p = \mu \nabla^2 \vec{u} \tag{2.7}$$

Equation (2.7) highlights the balance between the net pressure force and the net viscous force. Due to the geometric simplifications and the boundary conditions ($u = 0$ at $r = R$), the pressure driven motion, named Poiseuille flow, in the circular channel of radius $R\,[m]$ is parabolic across the diameter:

$$u = \frac{R^2 - r^2}{4\mu} \left(-\frac{dp}{dx} \right) = u_{max} \left(1 - \frac{r^2}{R^2} \right) \tag{2.8}$$

where u_{max} is the maximum velocity: $u_{max} = \frac{R^2}{4\mu} \left(-\frac{dp}{dx} \right)$ at $r = 0$. The Poiseuille flow is characterized by a parabolic velocity profile (see Figure 2.1): the velocity of flow in the center of the channel is greater than that toward the outer walls.

In contrast, electrically driven flow that is a useful alternative to pressure-driven flow of water, known as electro-osmotic flow (EOF), offers a flat velocity profile across the channel. The next step requires the calculation of the total volumetric
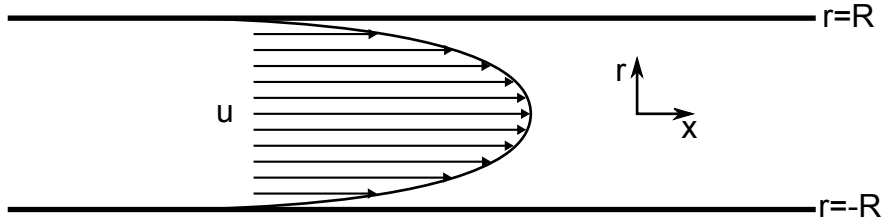

Figure 2.1: Parabolic velocity profile of the Poiseuille flow.

flow rate Q $[m^3/s]$ in the circular channel. In order to get it, we need to spacially integrate the velocity contributions (Equation (2.8)) from each lamina. Accordingly, the volumetric flow rate for the steady-state pressure-driven fluid flow in the channel, described by the Hagen-Poiseuille's law, becomes:

$$Q = \frac{\pi R^4}{8\mu} \left(-\frac{dp}{dx} \right).$$ (2.9)

Normalizing Equation (2.9) by the cross-sectional area, we generate the area-averaged velocity U $[m/s]$:

$$U = \frac{Q}{\pi R^2} = \frac{R^2}{8\mu} \left(-\frac{dp}{dx} \right).$$ (2.10)

To be precise, the Hagen-Poiseuille's law applies only for a channel that is perfectly straight and infinitely long. However, we can reasonably apply Equation (2.9) even to a channel with finite length L $[m]$ as long as this is by far the prevalent dimension of the geometry.

For most pressure-driven microfluidic devices, we can assume that the pressure gradient along the channel length is uniform. Then, we can approximate the term $-\frac{dp}{dx}$ to $\frac{\Delta p}{L}$, where Δp $[Pa]$ is the pressure difference through a finite channel length L. With this approximation, Equation (2.9) becomes simply:

$$Q = \frac{\pi R^4}{8\mu} \frac{\Delta p}{L}$$ (2.11)

where Q is defined as positive for flow from inlet to outlet.

Equation (2.11) gives the flow-pressure relation in pressure-driven channels and can be simplified as:

$$Q = \frac{\Delta p}{R_H} \qquad (2.12)$$

where the hydraulic resistance R_H $[Pas^3/m]$ is defined, for a cylindrical tube, as:

$$R_H = \frac{8\mu L}{\pi R^4}. \qquad (2.13)$$

In general, Equation (2.13) can be applied for non-circular channels, by replacing the channel radius R with the hydraulic radius r_H or diameter $D_H = 2r_H$. The hydraulic radius of the channel r_H $[m]$ is a geometric constant defined as $r_H = \frac{2A}{P}$, where A $[m^2]$ is the cross-sectional area of the channel and P $[m]$ is the wetted perimeter.

In microfluidic networks, most channel geometries are rectangular. For a rectangular microchannel with a low aspect ratio ($w \approx h$), the reciprocal of the hydraulic radius becomes the sum of the reciprocals of the channel width w $[m]$ and the channel height h $[m]$: $1/r_H = 1/w + 1/h$ or $r_H = wh/(w + h)$. However, this estimate gives about 20% error and thus it isn't much satisfying.

Actually, the solution to Equation (2.7) for a rectangular channel is quite complicated to derive, and it can be only calculated exactly as the summation of a Fourier series. The hydraulic resistance for the rectangular microchannel, in fact, is given by:

$$R_H = \frac{12\mu L}{wh^3 \left(1 - \frac{h}{w}\left(\frac{192}{\pi^5}\sum_{n=1}^{\infty}\frac{1}{(2n-1)^5}tanh\left(\frac{(2n-1)\pi w}{2h}\right)\right)\right)}. \qquad (2.14)$$

Note that when the aspect ratio is high[1] ($h/w < 1$), the Fourier series can be truncated at the first harmonica ($n = 1$ in Equation (2.14)) since the other terms become negligible and we obtain the simplified formula:

$$R_H = \frac{12\mu L}{wh^3}\left[1 - \frac{192h}{\pi^5 w}tanh\left(\frac{\pi w}{2h}\right)\right]^{-1}. \qquad (2.15)$$

This Equation is accurate to within 0.26% for any rectangular channel that has $\frac{w}{h} < 1$, provided that the Reynolds number Re is below 10^3.

Finally, by reversing Equation (2.12) and combining it with Equation (2.15), it results:

$$\Delta p = \frac{12\mu LQ}{wh^3}\left[1 - \frac{192h}{\pi^5 w}tanh\left(\frac{\pi w}{2h}\right)\right]^{-1}. \qquad (2.16)$$

---

[1]This condition is always verified in the microfluidic systems we considered.

which is the Hagen-Poiseuille's law we'll use hereafter to describe the flow in our rectangular microfluidic channels.

2.6 Rayleigh-Plateau instability

Rayleigh-Plateau instability explains why and how a falling stream of fluid breaks up into smaller drops. The driving force of the process arises from the intrinsic tendency of the liquids to minimize their surface area.

The explanation of this instability begins with the existance of tiny perturbations in the surface of the liquid. These are always present, no matter how smooth the stream is. If the perturbations are resolved into sinusoidal components, the equation for the radius of the stream can be written as: $r(z) = r_0 + A_k cos(kz)$, where r_0 is the radius of the umperturbated stream, A_k is the amplitude of the perturbation, z is the distance along the axis of the stream and k is the wave number (a measure of how many peaks and troughs per meter are present in the liquid surface). We thus find that some components grow with time while others decay with time. Among those that grow with time, some grow at faster rates than others. Whether a component decays or grows, and how fast it grows is entirely a function of its wave number k and the radius of the original cylindrical stream r_0.

By assuming that all possible components exist initially in roughly equal (but minuscule) amplitudes, the size of the final drops can be predicted by determining, through wave number, which component grows the fastest. As time passes, in fact, the component whose growth rate is maximum will come to dominate and will eventually be the one that pinches the stream into drops.

We observe that at the troughs the radius of the stream is smaller, hence, according to the Young-Laplace equation reported below, the pressure due to surface tension is increased:

$$\Delta p = \sigma(\frac{1}{r_1} + \frac{1}{r_2}) \tag{2.17}$$

where σ is the so called surface tension coefficient, r_1 is the radius of the stream and r_2 is the curvature of the sinusoidal wave describing the liquid surface profile. Likewise, at the peaks the radius of the stream is greater and, by the same reasoning, pressure due to surface tension is reduced.

If this were the only effect, we would expect that the higher pressure in the trough would squeeze liquid into the lower pressure region in the peak, understanding how the wave grows in amplitude with time. But the Young-Laplace equation is influenced by two separate radius coponents. In this case, one is the radius, already discussed, of the stream itself (r_1). The other is the radius of the curvature of the wave (r_2). Observe that the radius of curvature at the trough is negative meaning that, according to Yoiung-Laplace, it decreases the pressure in the trough. Likewise, the radius of curvature at the peak is positive and increases the pressure in that region. The effect of these components is in opposite with the action of the radius of the stream itself. The two phenomena, in general, do not exactly cancel. One of them will have greater magnitude than the other, depending upon wave number k and the initial radius of the stream r_0. In particular, when the wave number is such that the radius of curvature of the wave dominates the stream's one, such components will decay over time. Conversely, when the radius of the stream dominates the wave's curvature, such components grow exponentially with time and promote drops formation.

When all the math is done, it can be found that unstable components (ie, the components that grow over time) are only those where the product of the wave number with the initial radius is less than unity: $kr_0 < 1$.

2.7 Analogy between fluidic and electric circuit

It is quite intuitive to consider the flow of a fluid like the flow of electricity: indeed, the molecules of fluid in a hydraulic circuit behave much like the electrons in an electrical circuit. On this purpose, the present Section is intended to highlight the main physical similarities between microfluidic circuits and electric circuits, mapping the electric circuit elements and theory onto corresponding microfluidic circuit elements and models. This well-known hydraulic-electric circuit analogy can be straightforwardly used to prescribe the flow/pressure relation in complex microfluidic networks based on conventional electric circuit theory. Starting from the basics, in electronics, linear resistors are the simplest circuit element and their resistance $R_E[\Omega]$ is predetermined by physical parameters:

$$R_E = \frac{\rho_E L}{A} \tag{2.18}$$

where $\rho_E[\Omega m]$ is the reisistivity of the conductor, $L[m]$ is the length of the conductor and $A[m^2]$ is its cross-sectional area (see Figure 2.2(a)). The resistance of the resistors can be prescribed by Ohm's law:

$$V = R_E I \tag{2.19}$$

where $V[V]$ is the voltage across the conducting material and $I[A]$ is the current flowing through the conductor (see Figure 2.2(b)). This formulae and relations between voltage, current, electric resistance and conductor length are physically similar to those between pressure, flow, hydraulic resistance and channel length in a microfluidic context. In particular, Ohm's law (Equation (2.19)) finds its counterpart in the so called Hagen-Poiseuille's law (see Section §2.5):

$$\Delta p = R_H Q \tag{2.20}$$

where $\Delta p[Pa]$ is the pressure difference across a microfluidic channel, $Q[m^3/s]$ is the volumetric flow rate that crosses the channel and $R_H[Pa \cdot s/m^3]$ is the hydraulic resistance (see Figure 2.2(d)). Since we are interested in microfluidic channels of rectangular cross-section, the approximated formula for the hydraulic resistance to which we have to refer is the following:

$$R_H = \frac{a\mu L}{wh^3} \tag{2.21}$$

where $L[m]$ is the length of the channel, $w[m]$ is the width of the channel, $h[m]$ is the height of the channel and a is a dimensionless parameter defined as $a = 12[1 - \frac{192h}{\pi^5 w}tanh(\frac{\pi w}{2h})]^{-1}$ (see Figure 2.2(c)).

Continuing with the electric circuit analogy, if N fluidic resistors (microfluidic channels) are collectively arranged in series, an equivalent single fluidic resistor has a hydraulic resistance equal to the sum of the N hydraulic resistances:

$$R_{H,s} = R_{H,1} + R_{H,2} + ... + R_{H,N}. \tag{2.22}$$

This is due to series-connected fluidic resistors carrying the same volumetric flow from one terminal to the other. Similar simplification can be applied to parallel-connected fluidic resistors. In a circuit containing N fluidic resistors in parallel, the equivalent single fluidic resistor has a hydraulic resistance equal to the reciprocal of the sum of reciprocals of each hydraulic resistance:

$$\begin{aligned} R_{H,p} &= R_{H,1} \parallel R_{H,2} \parallel ... \parallel R_{H,N} \\ R_{H,p} &= \frac{1}{\frac{1}{R_{H,1}} + \frac{1}{R_{H,2}} + ... + \frac{1}{R_{H,N}}}. \end{aligned} \tag{2.23}$$
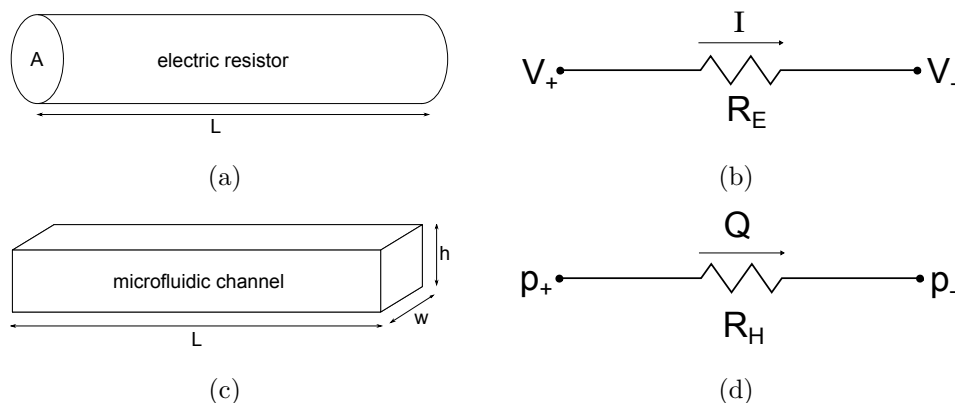
Figure 2.2: Physical similarities between the flow of a fluid in a rectangular microchannel and the flow of electricity in a resistor.

Another very useful fluidic/electric similarity concerns sources. Most pressure-driven microfluidic devices, in fact, need to be powered using external pressure sources. Conventionally, external pumps such as syringe and peristaltic pumps are widely used to supply constant fluid flow to devices. The volumetric flow supplied by the pumps is completely independent of the pressure drop across the inlet and outlet ports of a device. It cannot be known a priori the pressure drop across an independent fluid flow source, because it depends entirely on the equivalent hydraulic resistance of the circuit to which it is connected. In this case, an independent constant fluid flow source Q_S is analogous to an independent DC current source. Actually, in order to introduce the intrinsic non-ideality of the sources, we need also to consider an internal resistance $r_i \gg$ in parallel to the ideal current generator (see Figure 2.3).
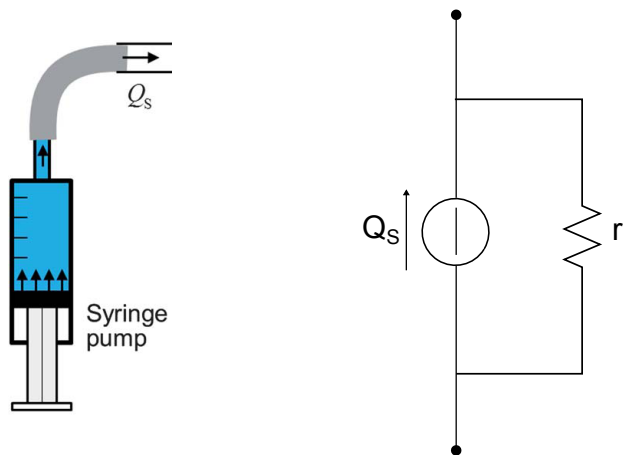

Figure 2.3: Analogy between constant fluidic flow source and current generator.

An alternative method is to connect an independent pressure source to inlet ports. Basically, the flow is controlled by the gravity-driven flow induced by the hydraulic head difference, $\Delta h[m]$, between the vertical source-inlet and drain-outlet reservoirs of microfluidic devices. For an independent and constant pressure source, Δh has to be held constant all the time. Alternatively, pressurized reservoirs connected with external pneumatic sources are used to provide independent, constant and controllable pressure to a device. The independent constant pressure source p_S is analogous to the corresponding independent DC voltage source. In this case the intrinsic non-ideality of the source is rendered once we add a series internal resistance $r_i \ll$ to the ideal voltage generator (see Figure 2.4).
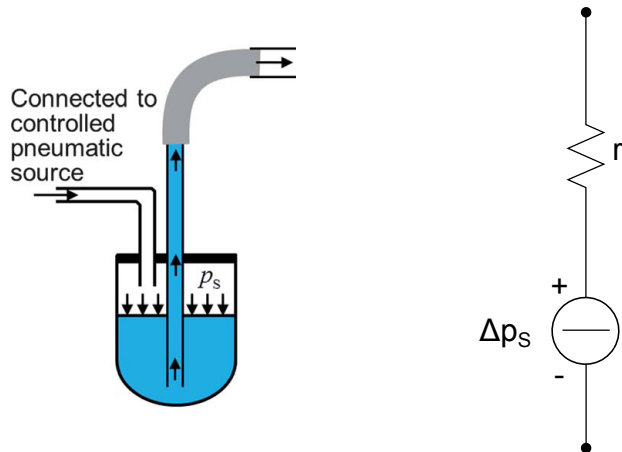

Figure 2.4: Analogy between constant fluidic pressure source and voltage generator.

Most microfluidic network-based devices, however, are fed with two or more pumping sources for the source-inlet ports (for example, continuous phase and dispersed phase pumps for droplet production) physically disconnected from the drain-outlet ports. In electric circuit analogy, the latter can be treated as earth or floating ground since the output port is normally open to atmosphere pressure p_{atm}.

Another fundamental concept in electric circuit theory concerns charge conservation which states that the algebraic sum of the currents entering any node is zero:

$$\sum_{n=1}^{N} I_n = 0. \tag{2.24}$$

This physical law is called Kirchhoff's current law (KCL). Similarly, the conservation of mass in fluidic circuits implies that the sum of the flows into a node should be equal to the sum of the flows leaving the node. Therefore the flow relation for the mass conservation at a node, analogous to KCL, is:

$$\sum_{n=1}^{N} Q_n = 0. \tag{2.25}$$

Energy conservation, instead, imposes that, in an electric circuit, the energy required to move a unit charge from point X to point Y must have a value independent of the path chosen to get from X to Y. Any route must lead to the same value for the energy or the voltage. We may assert this fact through Kirchhof's voltage law (KVL): the algebraic sum of the voltages around any closed path is zero

$$\sum_{n=1}^{N} V_n = 0. \tag{2.26}$$

Similarly, conservation of energy in fluidic networks implies that the sum of each pressure drop along the closed path is zero. Thus, the pressure drop relation for energy conservation in a closed path, analogous to KVL, is:

$$\sum_{n=1}^{N} \Delta p_n = 0. \tag{2.27}$$

Moreover, in electric circuit theory, the application of concepts such as voltage and current division can greatly simplify the analysis.

Voltage division is used to express the voltage across one of several series resistors in terms of the voltage across the series combination. Thus, if a microfluidic network includes N series fluidic resistors, we can apply this rule to obtain the general result for pressure division across the n-th fluidic resistor:

$$\Delta p_n = \frac{R_{H,n}}{R_{H,1} + R_{H,2} + ... + R_{H,N}} \Delta p_S \tag{2.28}$$

where $\Delta p_S = p_S - p_{atm}$ is the pressure drop across the inlet pump.

The dual of voltage division in electric circuit theory is current division. It is used to describe the current across one of several parallel resistors in terms of the current across the parallel combination. Transferring this rule to the analogous microfluidic circuit, if a total flow of Q_S is supplied to N parallel fluidic resistors,

then the volumetric flow rate Q_n through the fluidic resistor $R_{H,n}$ is given by:

$$Q_n = \frac{\frac{1}{R_{H,n}}}{\frac{1}{R_{H,1}} + \frac{1}{R_{H,2}} + ... + \frac{1}{R_{H,N}}} Q_S. \qquad (2.29)$$

Notice that smaller fluidic resistors in a parallel network carry proportionally larger flows, thus providing shortcut path-ways through microfluidic networks. This concept is very useful in droplet based networks since drops in a bifurcation normally follow the path at least resistance (see Chapter §4).

In order to provide a more immediate overview of the parallelism between microfluidic and electric circuits we collected in Table 2.1 the similarities discussed so far.

Microfluidics	Electronics
Fluid molecules	Electrons
Flow of fluid	Flow of electricity
Volumetric flow rate $Q[m^3/s]$	Electric current $I[A]$
Pressure drop $\Delta p[Pa]$	Voltage drop $\Delta V[V]$
Microchannel segment (fluidic resistor)	Conductive wire (electric resistor)
Hydraulic resistance $R_H[Pa \cdot s^3/m]$	Electric resistance $R_E[\Omega]$
Hagen-Poiseuille's law: $\Delta p = R_H Q$	Ohm's law: $V = R_E I$
Equivalent series fluidic resistors: $R_{H,s} = R_{H,1} + ... + R_{H,N}$	Equivalent series electric resistors: $R_{E,s} = R_{E,1} + ... + R_{E,N}$
Equivalent parallel fluidic resistors: $R_{H,p} = R_{H,1} \parallel ... \parallel R_{H,N}$	Equivalent parallel electric resistors: $R_{E,p} = R_{E,1} \parallel ... \parallel R_{E,N}$
External pump	Power supply or battery
Independent, constant fluid flow source	Independet, constant current generator
Independent, constant pressure source	Independet, constant voltage generator
Atmospheric pressure p_{atm}	Earth or floating ground
Law of mass conservation: $\sum Q_n = 0$ at a node	Kirchhof's current law (KCL): $\sum I_n = 0$ at a node
Law of energy conservation: $\sum \Delta p_n = 0$ in a closed path	Kirchhof's voltage law (KVL): $\sum V_n = 0$ in a closed path
Flow division	Current division
Pressure division	Voltage division

Table 2.1: List of physical similarities between microfluidics and electronics

It is worth to point out that we limited our analysis to the physical similarities which we're interested in assessing, but, actually, the fluidic/electric analogy

involves many other aspects[1].

If taken too far, however, the electric circuit analogy can create misconceptions when analyzing a microfluidic system. Recall that Ohm's law cannot explain the details of the miscroscopic transport of electrons in electrical systems. Rather, it describes an average effect (e.g., current flow) that is consistent with the net flux of electrons in a conductor. In the similar manner, Hagen-Poiseuille's law, analogous to Ohm's law, describes the average volumetric flow in a microchannel. Thus, the application of electric circuits methods to microfluidics does not provide detailed information about the flow field itself (e.g., the spatial distribution of the velocity field within a channel). Numerically based CFD simulations are reccomended to investigate the details of such behavior, expecially in 2D and 3D systems. The droplets based networks itself are examples where the electric circuit analogy must be verified carefully since there are multiple types of fluids (e.g., dispersed and continuous phase) but only one type of electron.

Chapter 3

Droplet generation

In the study of a microfluidic network, the first aspect to be analyzed is, of course, the method of generating and introducing droplets in the system. This is achieved through passive techniques which generate a uniform, evenly spaced, continuous stream. Not only should these devices produce a regular and stable monodisperse droplet stream, they also need to be flexible enough to easily provide droplets of prescribed volume at prescribed rates. To this end, three main approaches have emerged so far based on different physical mechanisms:

- breakup in co-flowing streams;

- breakup in elongational strained flows (flow focusing devices);

- breakup in cross-flowing streams (T-junction).

3.1 Breakup in co-flowing streams

The geometry of co-flowing devices is reported in Figure 3.1. It simply corresponds to a cylindrical glass tube that is coaxially aligned with a rectangular outer microchannel.

In this system, the dispersed phase is firstly produced by the thin internal round capillary and then enters through a nozzle into the main rectangular channel where the continuous phase flows. Here the inner fluid is subjected to the pressure due to the immiscible carrier fluid which, together with the viscous shear stresses, deforms it and eventually leads to droplet pinch off.
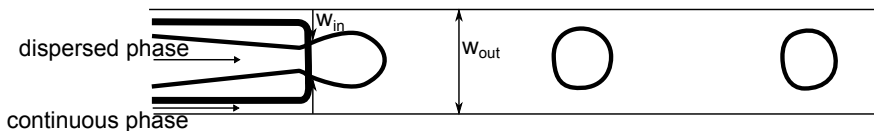
Figure 3.1: Example of droplet production in a co-axial injection device (top view).

As reported by Baroud *et al.* [2], two distinct regimes, concerning liquid breakup, has emerged in co-flowing streams devices: dripping, in which droplets pinch off near the capillary tube's tip, and jetting, in which droplets pinch off from an extended thread downstream of the nozzle. In both cases, the physics at the origin of droplet production is related to a sort of Rayleigh-Plateau instability (see Section §2.6). In particular, the transition from dripping to jetting can be interpreted as a transition from an absolute to a convective instability. This phenomenon occurs when the continuous phase velocity increases above a critical value U^*. Recent studies [3] pointed out how this threshold decreases as the flow rate of the dispersed phase increases and reported its further dependence on the viscosity of the inner and outer flow, as well as on the interfacial tension between the two phases.

The co-flowing system for droplet production, however, shows a considerable weak point if applied in soft lithography Lab on Chips (LoCs), which are nowadays the most common microfluidic devices. The cylindrical geometry of the injector, in fact, is a serious obstacle to its implementation in LoCs since the latter present a typical rectangular cross sectional geometry. In contrast, the two alternative geometries of flow focusing and T-junction are well suited to planar geometries but introduce more complex fluid dynamics, as detailed below.

3.2   Breakup in elongational strained flows

The typical geometry of flow focusing devices is depicted in Figure 3.2.

As can be appreciated, the dispersed stream, once injected into the system through a rectangular microchannel, is immediately squeezed by two counter-flowing streams of the continuous phase. The pressure exerted, in this way, by the continuous flow on the interface with the dispersed stream leads to the progressive
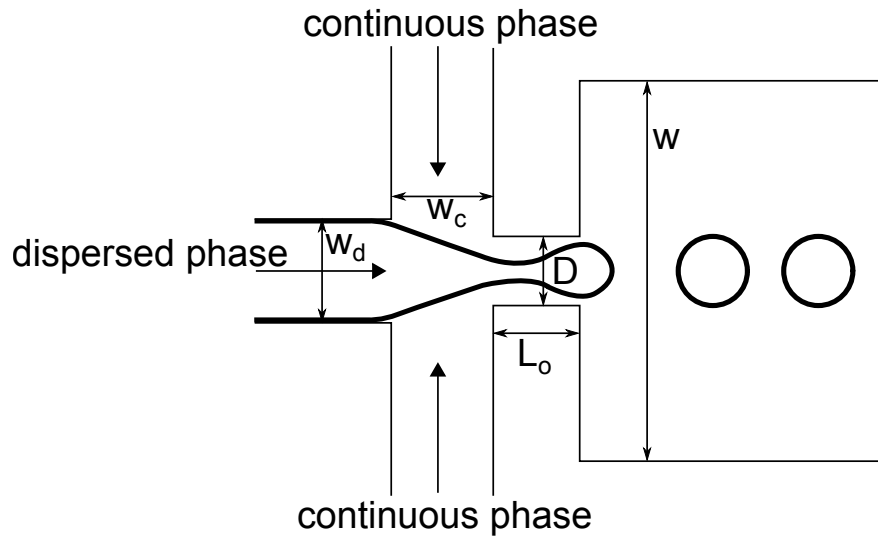
Figure 3.2: Example of droplet production in a flow-focusing device (top view).

thinning of the latter until breakup occurs. The droplet thus generated passes through an orifice of width D and length L_o and is then conveyed in a collector channel of width w.

Given the complexity of the device, many geometrical parameters play a role in this system. Above these, five main quantities can be identified: the width of the continuous phase's inlet channels w_c, the width of the dispersed phase's inlet channel w_d, the length of the orifice L_o and its width D, as well as the collector channel width w. As these parameters are varied, four regimes can be observed: squeezing, dripping, jetting and thread formation. However, the large number of geometrical aspect ratios characterizing flow-focusing devices has prevented the determination of simple scaling laws to predict the transition between various regimes, the droplet size, distribution and rate of emission as a function of the key parameters previously mentioned.

Recent velocity field measurements[4] suggest that the squeezing phenomenon is governed by the build up of a pressure difference as the advancing finger partially blocks the outlet channel, via a mechanism very similar to the one we will see in more details in T-junctions. Other reports[5], however, state that squeezing/dripping droplet breakup depends solely on the upstream geometry and associated flow field, and not on the geometry of the channel downstream of the flow focusing orifice. By contrast, the elongation and breakup of the fine

thread during the thread formation mode of breakup seems to depend solely on the geometry and flow field in the downstream channel. In light of these papers and despite the widespread use of flow-focusing devices, it is clear that the understanding of their detailed dynamics still warrants further research.

These issues, combined with the drawbacks already underlined for the co-flowing devices, led us to choose the T-junction as the method for droplet production in our analyses and simulations of microfluidic circuits. Indeed, the mechanism of breakup in cross-flowing stream (T-junction) has none of the disadvantages emerged for co-flowing and flow-focusing devices: it is well suited for planar geometries and has clear-cut scaling laws for its physical behavior.

Let us, then, examine carefully this method for droplet generation.

3.3   Breakup in cross-flowing streams

Figure 3.3 illustrate the geometry of a T-junction. Very simply, it consists of two channels merged at right angle. The main channel carries the continuous (or carrier) fluid and the orthogonal channel supplies the fluid that will be dispersed (hereafter dispersed or discontinuous fluid). The channels have rectangular cross sections, and there are only three geometrical parameters that define completely the size and shape of the T-junction: the width w_c of the main channel, the width w_d of the channel supplying the discontinuous fluid and the height h of the channels. In this regard, we focused on planar geometries, with identical rectangular cross-section for every channel, in which the width is slightly greater than the height. Liquid flows are commonly controlled via independent syringe pumps imposing the inlet volumetric flow rates Q_c and Q_d for each phase.
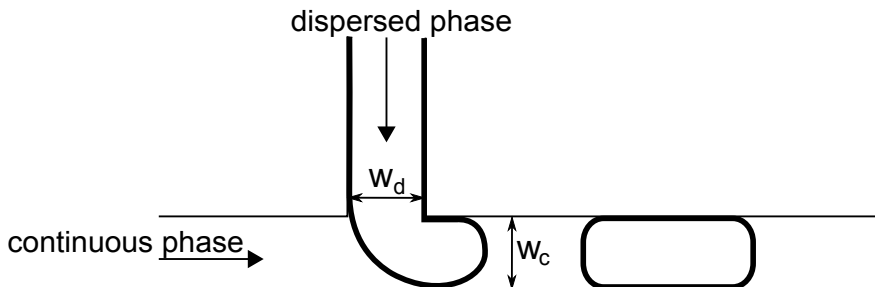

Figure 3.3: Example of droplet production in a T-junction (top view).

3.3.1   Forces anlysis

The process of droplet formation actually begins as soon as the dispersed phase starts penetrating into the outer channel. Here, three main forces act on the emerging interface and influence droplet breakup: the viscous shear-stress force (F_τ), the surface (or interfacial) tension force (F_σ) and the force arising from the increased resistance to flow of the continuous fluid around the tip (hereafter "squeezing force", F_S). The understanding of their balance is crucial for drawing the correct model of the breakup process so, in the next paragraphs, we will examine, one by one, the contribution given by these forces during droplet generation.

Viscous shear-stress force   A viscous shear stress is defined as the component of stress co-planar with a material cross section. In our case, this kind of stress is exerted on the dispersed phase by the cross-flow of the continuous phase. Its magnitude is estimated by the product $\mu_c G$, where μ_c is the viscosity of the carrier fluid and G is a characteristic rate of shear strain that is proportional to Q_c and is a function of the T-junction and the emerging interface geometry. More in detail, we can approximate this stress as $\tau = \mu_c u_{gap}/\epsilon$, where $u_{gap} = Q_c/(h\epsilon)$ is the speed of the continuous fluid flowing through the gap, of characteristic thickness ϵ, between the interface and the wall of the channel (see Figure 3.4). In order to estimate the net force acting on the immiscible tip, we then multiply the shear stress $\tau = \mu_c Q_c/(h\epsilon^2)$ by the surface area of the interface in the gap $A_{gap} \sim hw^1$, where we take w as the characteristic axial length-scale of the tip (see Figure 3.4). Finally, the corresponding net force on the tip is pointed downstream and has the magnitude of:

$$F_\tau \approx \mu_c Q_c \frac{w}{\epsilon^2}. \tag{3.1}$$

Squeezing force   The so called squeezing force comes into play when the thread of the discontinuous fluid almost obstructs the cross section of the main channel (see Figure 3.4). In this situation, the available area through which continuous fluid can pass is significantly restricted leading to an increased pressure directly upstream of the junction. As detailed below, the magnitude of the squeezing

---

[1]The shear stress, in fact, is given by the ratio between the force applied and the surface affected by the stress $\tau = \frac{F_\tau}{A}$.
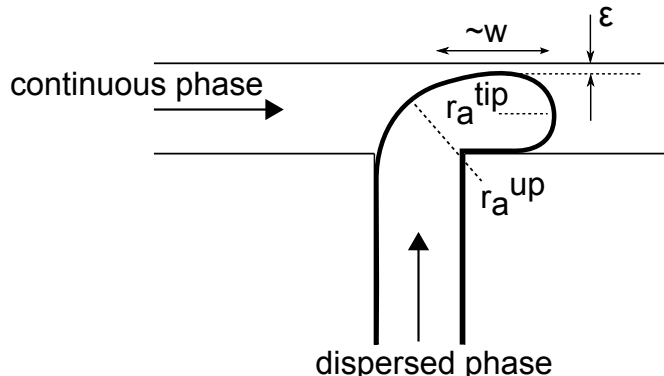
Figure 3.4: Schematic illustration (top view) of the shape of the immiscible thread's tip at an intermediate stage of break-up in a T-junction.

pressure increases dramatically as the distance between the emerging interface and the opposing wall of the main microchannel (ϵ) decreases. For $\epsilon \sim w$, using the Hagen-Poiseuille's law referred to a rectangular channel (see Section §2.5), we can estimate the pressure drop Δp over the length ($\sim w$) of the immiscible tip: $\Delta p \approx \mu_c Q_c w / (h^2 \epsilon^2)$. When $\epsilon \ll w$, instead, we evaluate Δp for a thin film of typical thickness ϵ, width h and length w (Figure 3.4): $\Delta p \approx \mu_c Q_c w / (h \epsilon^3)$, and the corresponding net force obtained, oriented downstream, is equal to:

$$F_S \approx \Delta p h w = \mu_c Q_c \frac{w^2}{\epsilon^3}. \tag{3.2}$$

The exact value of the exponent n to which the thickness of the film ϵ should be raised in the above expression can be derived from a detailed lubrication analysis[6] for flow around objects near-filling the cross-sections of capillaries: n depends on the geometry of the cross-section of the capillary and on the geometry and material parameters of the object. Importantly, n is larger than 2 and consequently we can expect that $F_S > F_\tau$ when $\epsilon \ll w$.

Interfacial tension force Surface tension is a contractile tendency of the surface of a liquid that allows it to resist an external force. The cohesive forces among liquid molecules are responsible for the phenomenon of surface tension. Very simply, it can be interpreted as follows: in the bulk of the liquid, each molecule is pulled equally in every direction by neighboring molecules, resulting in a net force of zero. The molecules at the surface, differently, are not surrounded by similar molecules on all sides and therefore are pulled inwards.

In our case, in particular, the surface tension is ruled by the interaction between dissimilar liquid (dispersed and continuous phase). This kind of surface tension is called interfacial tension, but its physics are almost the same. It resists deformation due to continuous fluid by establishing a pressure jump across the curved edge of the growing droplet. In particular, the surface tension force is associated with the Laplace pressure jump Δp_L across a static interface, $\Delta p_L = \sigma(r_a^{-1} + r_r^{-1})$ where σ is the interfacial tension coefficient (sometimes denoted γ), r_a is the axial curvature (in the plane of the device) and r_r is the radius of the radial curvature (in the cross-section of the neck joining the inlet for the discontinuous fluid with the tip). In the intermediate stage of the process of formation of a droplet (Figure 3.4) the radial curvature is bounded by the height of the channels ($h < w$) and $r_r \approx h/2$ (or less) everywhere. The axial curvature is more emphasized at the downstream tip of the immiscible thread ($r_a^{tip} \approx w/2$) than at the upstream side of it ($r_a^{up} \approx w$): the interface on the downstream side of the thread acts on the liquid inside the thread with a stress $p_L \approx -\sigma(2/w + 2/h)$ (the minus sign signifies that the stress is oriented upstream), and the interface located upstream acts on the discontinuous liquid with a stress $p_L \approx \sigma(1/w + 2/h)$ (oriented downstream). The sum of the two, multiplied by the cross-section of the channel gives the following estimation of the interfacial tension force:

$$F_\sigma \approx -\sigma h, \tag{3.3}$$

which has a stabilizing effect on the tip: in the absence of any other stresses or forces, surface tension would position the tip symmetrically about the axis of the inlet channel for the dispersed phase.

To summarize the order-of-magnitude estimates of the forces acting on the tip, we note that the only stabilizing force arises from the interfacial tension effects (see Equation (3.3)). On the other hand, there are two destabilizing forces (see Equation (3.2) and (3.1)), both of which increase sharply upon the decrease of the separation ϵ between the interface and the opposing wall of the main channel.

As stated by several studies[7, 8, 9], the balance of these forces leads to the definition of two principal regimes of breakup in T-junction:

- *squeezing regime*;

- *dripping regime*.

Importantly, the transition between them is governed by the Capillary number (Ca) which is a dimensionless parameter that describes the relative magnitude of the viscous shear stress compared with the interfacial tension (see Section §2.2). A simple definition for Ca in microfluidics is given in terms of the average velocity u_c of the continuous phase, the dynamic viscosity μ_c of the continuous phase and the interfacial tension coefficient σ:

$$Ca = \frac{\mu_c u_c}{\sigma} = \frac{\mu_c Q_c}{\sigma w h}. \tag{3.4}$$

In particular, for low values of the Capillary number ($Ca < Ca_{CR}$), ie when the interfacial forces dominate the shear stress, the dynamics of breakup of immiscible thread in T-junction is dominated by the squeezing force across the droplet as it forms (squeezing regime). In the opposite case ($Ca > Ca_{CR}$), the shear stress starts playing an important role and the system starts operating in the so called dripping regime. As reported in recent papers[8] and confirmed in our numerical simulations, this threshold is given by:

$$Ca_{CR} \approx 10^{-2}. \tag{3.5}$$

Let us now examine in more detail the two regimes mentioned above with a particular focus on the squeezing regime which is the one we will adopt later on for our microfluidic networks because it shows the best flexibility and controllability over the shape of the droplets generated.

3.3.2 Squeezing regime

The typical process of droplets formation via squeezing regime is visually depicted in the simulation of Figure 3.5 where the principal geometrical and physical parameters imposed are the following: $h = 50\mu m, w_c = w_d = 150\mu m, Q_c = 3.75 nL/s, Q_d = 1.875 nL/s$. Keeping it in mind and on the basis of the previous analysis and observations, the mechnism in question can be briefly described as follows: the two immiscible fluids form an interface at the junction of the dispersed inlet channel with the main channel. The stream of the discontinuous phase starts penetrating into the main channel and a droplet begins to grow under the effect of the viscous shear-stress force (Figure 3.5(a)). The latter, however, is not sufficient to distort the interface significantly because this operating regime works under the condition $Ca < Ca_{CR} \Rightarrow$ interfacial tension dominates

shear stress. Consequently, the emerging droplet manages to fill the junction and restricts the available area through which continuous fluid can pass, leading to an increased pressure directly upstream of the junction (Figure 3.5(b)). When the corresponding squeezing force overcomes the interfacial tension force, the neck of the emerging droplet squeezes (Figure 3.5(c)), promoting its breakup. Finally, the disconnected liquid plug flows downstream of the main channel, while the tip of the dispersed phase retracts to the end of the inlet and the process repeats (Figure 3.5(d)). The intrinsic high reproducibility shown by this mechanism is fundamental for the stable production of uniform droplets with identical length and shape (Figure 3.5(e)) over a wide range of flow rates. This is also the reason why we chose to work under squeezing regime in our simulations of T-shaped droplet inlet systems.
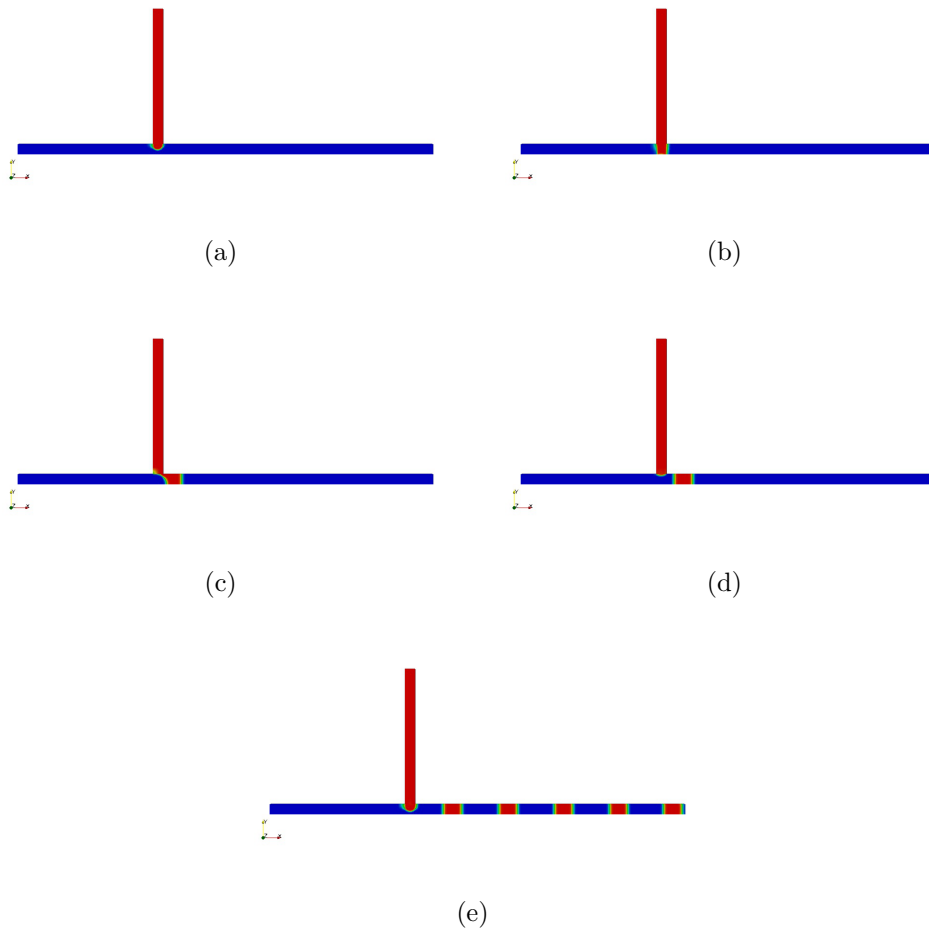

(a)   (b)

(c)   (d)

(e)

Figure 3.5: Typical process of droplet formation in squeezing regime.

Droplets length   Applying the model of evolution of breakup at the T-junction in the squeezing regime presented so far, Garstecki *et al.*[8] obtain a simple formula for the length L_d of the resulting droplets:

$$L_d = w(1 + \alpha \frac{Q_d}{Qc}) \qquad (3.6)$$

where w is the width of the main channel, Q_d is the flow of the dispersed phase, Q_c is the flow of the carrier fluid and α is a dimensionless parameter of order one. Equation (3.6) can be intuitively understood by arguing that detachment begins once the emerging discontinuous thread fills totally the main channel, i.e. when the squeezing force is stronger. At this moment, the length of the droplet is approximately equal to the width of the channel w and the thickness of the neck in the junction starts decreasing at a rate which depends on the mean speed of the continuous fluid u_c. So, the flow of the carrier fluid ($Q_c = u_c hw$) sets the time for the growth of the droplet because it determines the "squeezing time" necessary for the neck to break. This results in an inverse proportionality between droplet length and continuous phase flow ($L_d \propto \frac{1}{Q_c}$). In fact, considering an equal input discontinuous phase flow, the greater the continuous flow the lower the squeezing time and thus the length of the resulting droplets. On the other hand, there is a direct proportionality between droplet length and dispersed phase flow ($L_d \propto Q_d$) because Q_d determines how much discontinuous fluid manages to flow in the droplet before the squeezing time imposed by the flow of the carrier fluid ends and breakup occurs.

Interdistance between droplets   Another physical parameter to be considered, that'll be useful later on, concerns the spacing $\delta[m]$ between droplets generated in squeezing regime. Its scaling relation can be deduced, as reported below, thanks to the application of the mass conservation law.

Let us consider a sufficiently long time τ and the related distance $x = u'_d\tau$ along the main channel (being u'_d the velocity of the dispersed fluid in the main channel). The number of droplets along x in the time interval τ is given by:

$$n_d(\tau) = \frac{x}{L_d + \delta} = \frac{u'_d\tau}{L_d + \delta}, \qquad (3.7)$$

where L_d is the length of the single droplet and δ is the interdistance between them (see Figure 3.6).
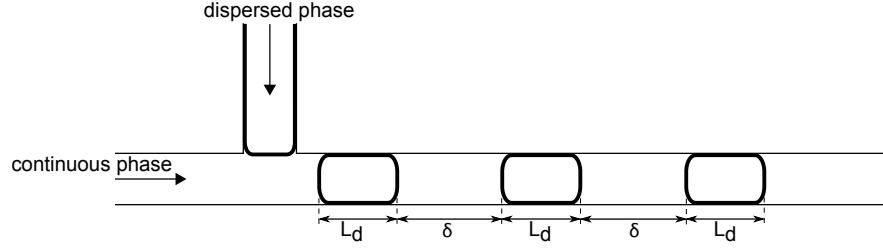
Figure 3.6: Schematic illustration of a train of droplets created by a T-junction.

Now, the mass conservation law imposes that the volume of dispersed liquid injected by the discontinuous phase inlet channel throughout the time interval τ ($Vol_{d,in} = Q_d\tau = u_d wh\tau$) corresponds to the volume of dispersed fluid along x in the main channel ($Vol_{d,x} = L_{droplet} whn_d = L_d wh\frac{u'_d\tau}{L_d+\delta}$):

$$u_d wh\tau = L_d wh\frac{u'_d\tau}{L_d + \delta} \Rightarrow u_d(L_d + \delta) = L_d u'_d. \tag{3.8}$$

The next step requires the evaluation of the velocity of the dispersed fluid in the main channel u'_d. To determine it, we make the hypothesis that dispersed and continuous phase flow at the same velocity ($u'_d = u'_c = u$) in the main channel, though it is not always true[10]. Then, we can exploit the parallelism that exist between the microfluidic and electrical circuit (see Section §2.7) as reported in Figure 3.7: in particular, we can associate the flow of the fluids (Q_d, Q_c, Q) in the microchannels of the T-junction to the current in the analogous electrical circuit (I_d, I_c, I). In this way, by applying Kirchhoff's law we obtain $I = I_d + I_c$ and thus:

$$Q = Q_d + Q_c \Rightarrow u = u_d + u_c.^2 \tag{3.9}$$

Substituting Equation (3.9) in (3.8), it results:

$$u_d(L_d + \delta) = L_d(u_d + u_c) \Rightarrow \delta = L_d\frac{u_c}{u_d} = L_d\frac{Q_c}{Q_d}. \tag{3.10}$$

Finally, replacing (3.6) in (3.10), we obtain the desired formula for the interdistance between droplets generated in a T-junction in the squeezing regime:

$$\delta = \frac{Q_c}{Q_d}w(1 + \alpha\frac{Q_d}{Q_c}). \tag{3.11}$$

---

[2] The last implication follows from the fact that we always consider channels with identical cross section.
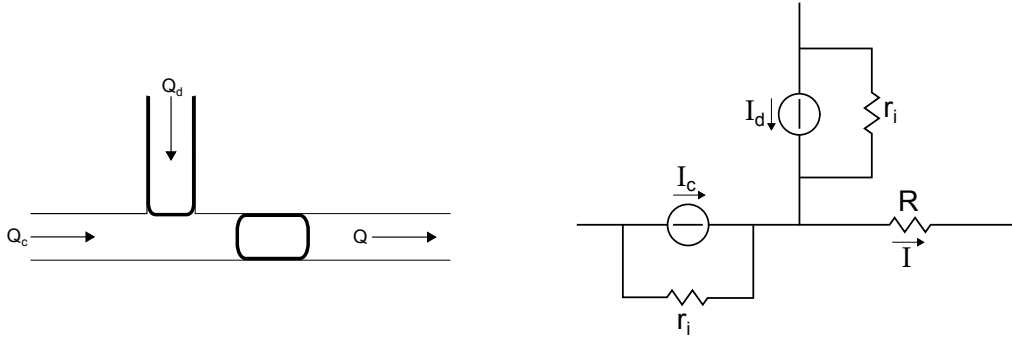
Figure 3.7: Analogy between microfluidic T-junction and electric circuit.

Lingering on Equation (3.10), it can be noted that droplets length and inter-distance are strictly correlated since δ depends on L_d. Consequently, once fixed the geometry of the system and the physical parameters of the liquids, bubbles with a specific length will have a corresponding precise interdistance between them. In order to decorrelate the two values and make δ independent of L_d the solution proposed by Jullien *et al.*[11] can be adopted. Basically, it consists in arranging, downstream of the T-shaped droplet generator, a series of small entries forming a comb (see Figure 3.8) which injects additional continuous phase, separating the droplets by variable lengths, typically several hundred of micrometers. On the contrary, if we want to near the bubbles, the comb can be employed to eject part of the continuous fluid between the droplets. In this way, we are able to modulate droplet interdistance irrespective of their length.
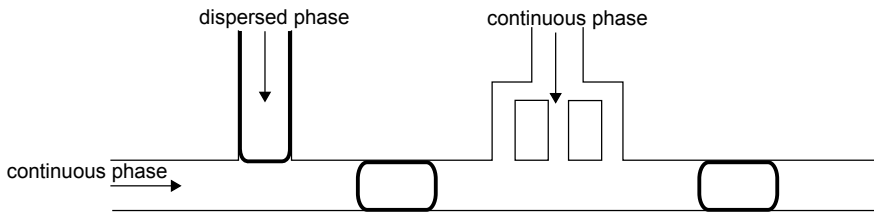

Figure 3.8: Sketch of droplet generator and comb to modulate droplet interdistance.

Simulations and numerical results In order to validate the theoretical analysis presented so far, we made use of the cfd software OpenFOAM (see Appendix A) to implement a T-junction device for droplet generation. The microchannels geometries imposed in our simulations are listed in Table 3.1 while in Table 3.2

are reported the common physical properties of the fluids considered.

System geometry	
Channels' height h	50 μm
Main channel's width w_c	150 μm
Dispersed channel's width w_d	150 μm

Table 3.1: Geometrical properties of the reference system

Fluids' properties		
Continuous phase→water	Dynamic viscosity μ_c	1.002 $mPa \cdot s$
	Density ρ_c	1000 Kg/m^3
	Kinematic viscosity ν_c	1.002 mm^2/s
Dispersed phase→silicone oil	Dynamic viscosity μ_d	145.5 $mPa \cdot s$
	Density ρ_d	970 Kg/m^3
	Kinematic viscosity ν_d	150 mm^2/s
Interfacial tension coefficient σ		46 mN/m

Table 3.2: Physical properties of the fluids considered

For this reference system, we plot the droplet length and interdistance as a function of the flow rate ratio $\varphi = Q_d/Q_c$ obtained in our simulations. In particular, we selected three different fixed inlet velocities for the continuous phase, namely $u_c = k \cdot u_{c,st}$ $[m/s]$ such that $Q_c = k \cdot whu_{c,st}$ $[m^3/s]$ with $u_{c,st} = 0.0005$ m/s and $k = 0.5, 1, 2$ and collected the relative results in Figure 3.9, 3.10 and 3.11 respectively. For each fixed continuous flow, the quantity $\varphi = Q_d/Q_c$ is varied in the range from 0.25 to 6.5 by opportunely incrementing the dispersed phase inlet flow Q_d. The simulative data (denoted by markers in the graphs) agrees very well, both for droplet length and droplet interdistance, with the theoretical model (continuous lines in the figures) expressed in Equations (3.6) and (3.11).

In addition, in Figure 3.12 we reported all together the graphs obtained for the three cases under examination. Analyzing the latter, it transpires the dependence of the fitting parameter α of Equation (3.6) from the absolute velocity set for the continuous phase. The various slopes obtained for the theoretical curves, in fact, denote different values of the prameter α: in particular, an increase in u_c corresponds to a decrease in α.
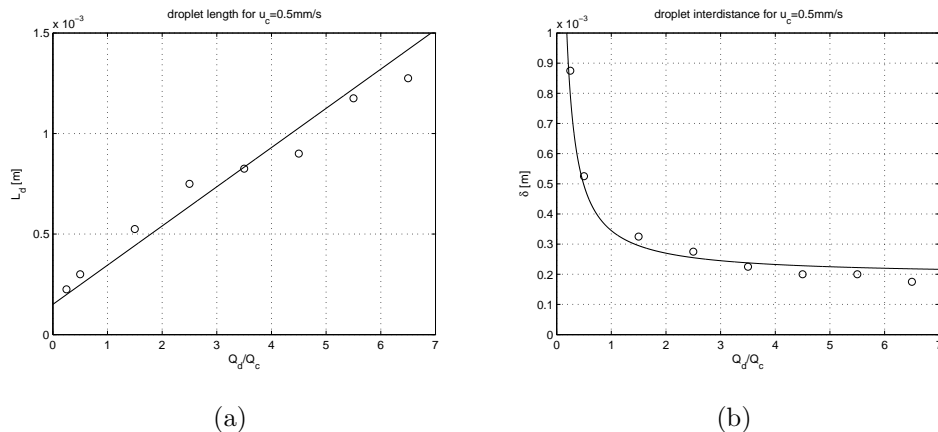
Figure 3.9: (a) Length and (b) spacing between droplets produced in a T-junction for a fixed value of $u_c = 0.5mm/s \Rightarrow Q_c = 3.75nL/s$. Continuous lines represents the theoretical curves obtained from (a) Eq. (3.6) and (b) Eq. (3.11) with $\alpha = 1.3$. Markers corresponds to the simulative results obtained with OpenFOAM.
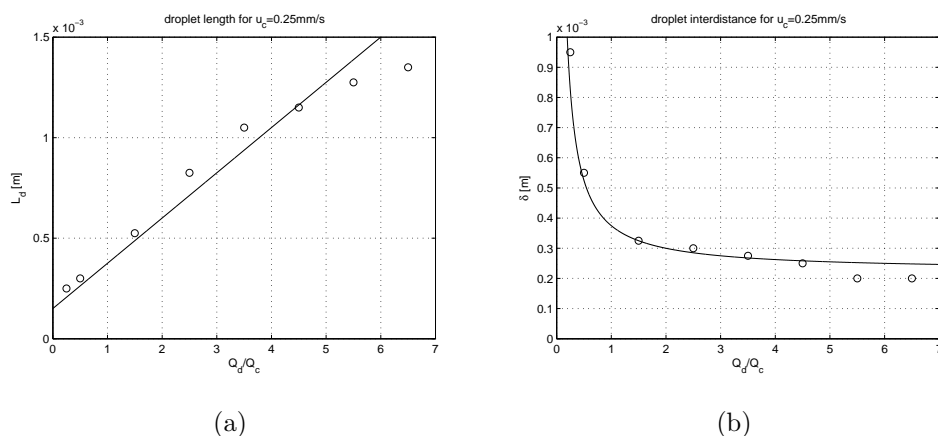

Figure 3.10: (a) Length and (b) spacing between droplets produced in a T-junction for a fixed value of $u_c = 0.25mm/s \Rightarrow Q_c = 1.875nL/s$. Continuous lines represents the theoretical curves obtained from (a) Eq. (3.6) and (b) Eq. (3.11) with $\alpha = 1.5$. Markers corresponds to the simulative results obtained with Open-FOAM.
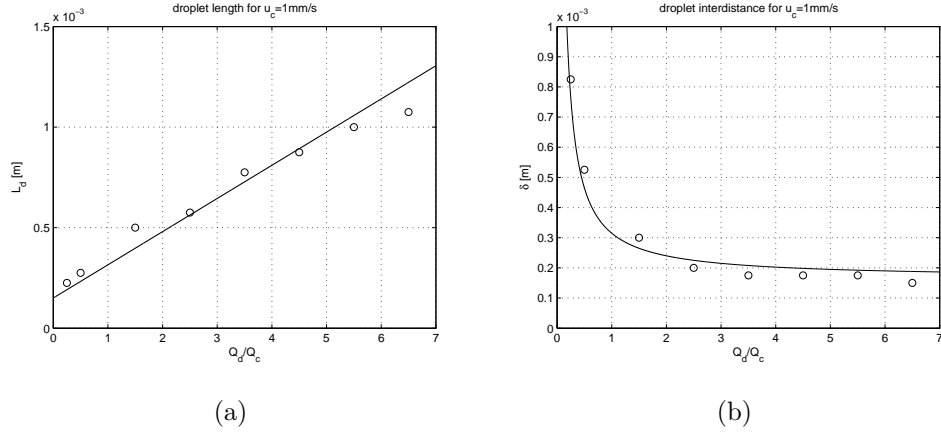
Figure 3.11: (a) Length and (b) spacing between droplets produced in a T-junction for a fixed value of $u_c = 1mm/s \Rightarrow Q_c = 7.5nL/s$. Continuous line represents the theoretical curves obtained from (a) Eq. (3.6) and (b) Eq. (3.11) with $\alpha = 1.1$. Markers corresponds to the simulative results obtained with OpenFOAM.
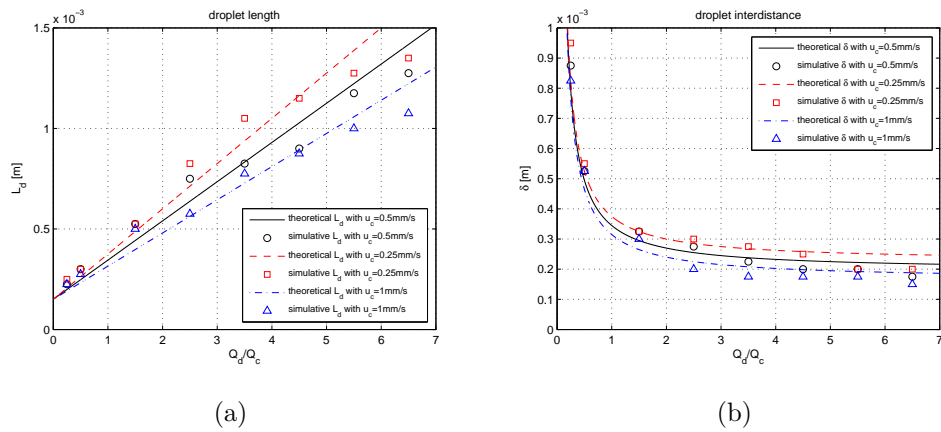

Figure 3.12: Collection and comparison of the data (a) from Figure 3.9(a), 3.10(a), 3.11(a) and (b) from Figure 3.9(b), 3.10(b), 3.11(b).

Finally, we noted that for low values of $\varphi = Q_d/Q_c$ the numerical results follows almost ideally our model while non linearity and anomalous behaviors emerge as soon as φ is increased too much. Indeed, when $Q_d > 7Q_c$ the squeezing regime further evolves in a sort of "parallel flow" regime, visually represented in the simulation of Figure 3.13 where the parameters considered are $h = 50\mu m, w_c = w_d = 150\mu m, Q_c = 3.75nL/s, Q_d = 37.5nL/s$. Remembering Equations (3.6) and (3.11), this simulative evidence, translates in an upper bound for the droplet length and in a lower bound for the droplet interdistance achievable once imposed the reference geometry.
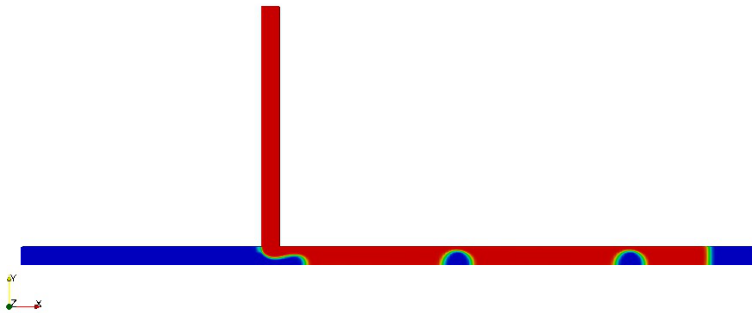

Figure 3.13: Degeneration of squeezing regime for high values of $\varphi = Q_d/Q_c$.

3.3.3 Dripping regime

As already stated, the dripping regime occurs when we work under the condition $Ca_{CR} > 10^{-2}$. In this case, contrary to the squeezing regime, droplet formation is entirely due to the action of the shear stress which is large enough to overcome the interfacial tension, analogous to spherical droplet breakup.

The typical mechanism of bubble production under dripping regime is illustrated step by step in the simulation reported in Figure 3.14 (the reference system considered here has got $h = 50\mu m, w_c = w_d = 150\mu m$, the continuous phase is characterized by $\mu_c = 145.5\ mPa \cdot s$ and $Q_c = 7.5nL/s$ while for the dispersed phase we imposed $\mu_c = 1.002\ mPa \cdot s$ and $Q_d = 7.125nL/s$). As soon as the dispersed phase enters the main channel (Figure 3.14(a)), it is affected by the

strong viscous shear-stress force F_τ caused by the carrier fluid. Accordingly, the emerging interface is sensitively distorted (Figure 3.14(b))and droplets are emitted before they can block the main channel (Figure 3.14(c)). This physical behavior, however, involves a strong limitation on the production of droplet which will consequently always be shorter than the width of the main channel w. For the same reason, the frequency of production of droplets is much higher than the corresponding one in the squeezing regime. This closeness between droplets can, in the worst case, entail the fusion of the same in the outer channel.

(a)   (b)
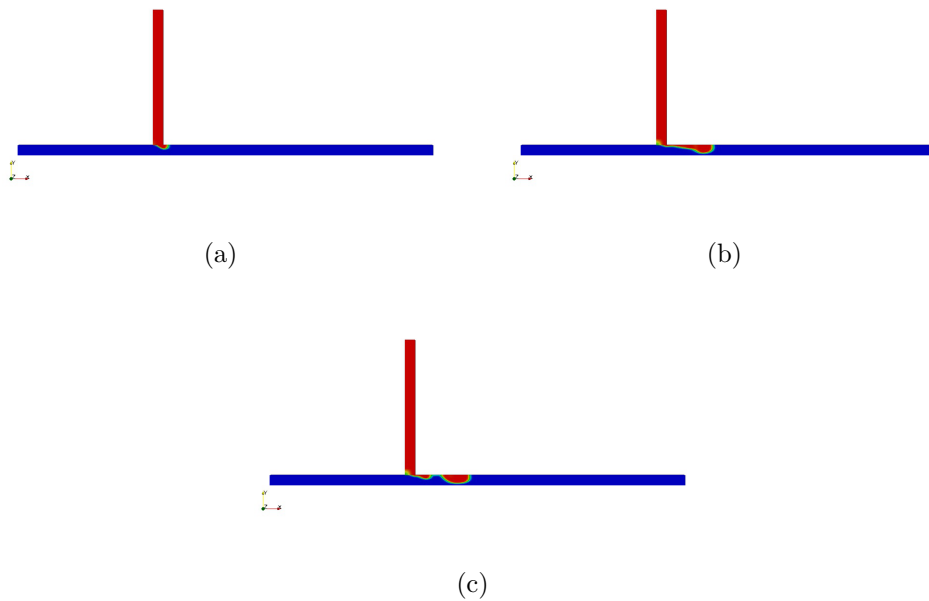

(c)

Figure 3.14: Typical process of droplet formation in dripping regime.

Scaling models[2] developed to describe this process also demonstrate that the droplet size depends predominantly on the capillary number Ca and not on the flow rate ratio φ: de facto, it decreases strongly as the capillary number increases. Furthermore, larger viscosity ratios $\lambda = \frac{\mu_d}{\mu_c}$ lead to smaller droplets.

As long as the inlet velocities imposed for the continuous and dispersed phase are quite low ($u_c, u_d < 10^{-2}$), our simulations agrees well with the theoretical background presented (see Figure 3.14 for a practical example). At greater orders of magnitude, instead, we observed that the dripping regime evolves into the formation of stable parallel flowing streams, as reported in Figure 3.15 for a reference system with $h = 50\mu m, w_c = w_d = 150\mu m, Q_c = 97.5nL/s, Q_d = 71.25nL/s$. We conjecture that the origin of this phenomenon lies in the fact

that, for the reference velocities, the frequency of droplet production is so high that it degenerates in a continuous stream.
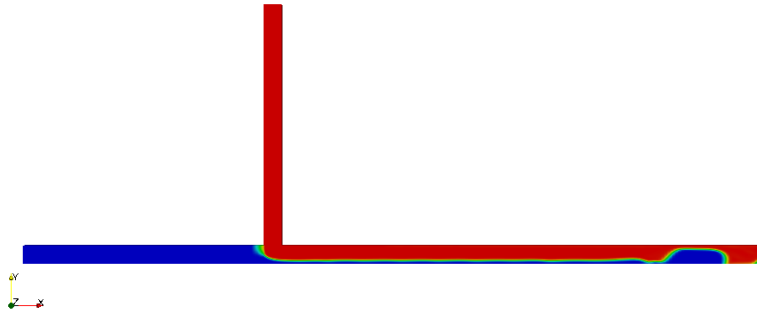

Figure 3.15: Degeneration of dripping regime for high values of u_d and u_c.

Chapter 4

Characterization of droplet dynamics in a bifurcating channel

After analyzing in detail the process of droplets generation, the next topic to be addressed, in order to understand the complex dynamics at the basis of microfluidic systems, concerns the behavior of droplets once they meet a bifurcation along the network.

Our interest in understanding the physics governing droplet dynamics in bifurcating channels, stem from the fact that we wish to convey droplets to the microfluidic machines. The latters are, in fact, physically connected to the network by means of ramifications.

On this purpose, we'll divide the present chapter in two main section: in the former one we are going to outline the so called droplet's breaking/non-breaking regions while in the latter we are going to point out how to passively pilot the droplets in a specific target arm of the bifurcation.

4.1   Droplet breakup in a bifurcating channel

If we consider the droplets, in analogy with the world of telecommunications, as the "packets" we want to deliver to the "end users" (microfluidic machines) of our network, we need to preserve their integrity throughout the entire system and, thus, even when they pass through "sensitive points" such as bifurcating channel.

Several studies, numerical simulations and experimental evidencies[12, 13, 14]

have been published in literature on this subject. Most of the studies focus on the T-junctions, where a channel splits into two symmetric arms, forming a T. In such systems, as we are going to formalize, depending on droplet size, capillary number and viscosity ratio of the dispersed and continuous phase, droplets arriving at the junction may either split or flow completely along one of the arm of the T.

Hereafter, we'll seek in particular to define the parameter range that controls the transition between breaking and non-breaking regime. Proceeding with order, we now describe the physics behind breakup and non-breakup regimes.

4.1.1   Breakup regime

Figure 4.1 describes the temporal droplet evolution obtained from a simulation characterized by the reference geometrical and physical parameters listed in Tables 3.1 and 3.2 and an inlet velocity of $u_c = 0.00075 m/s$.

(a)   (b)

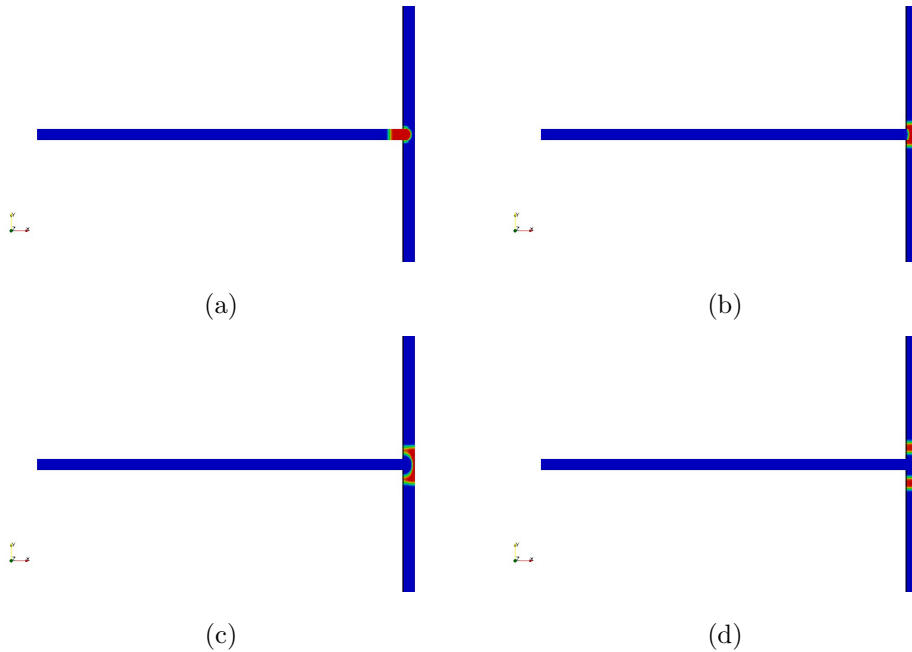(c)   (d)

Figure 4.1: Typical droplet dynamics in breakup regime at the bifurcation.

Figure 4.1(a) shows the elongated droplet as it is just about to come in contact with the edge of the junction. Immediately, it deforms symmetrically forming two identical liquid fingers in the upper and lower branch, which almost completely fill the channel (see Figure 4.1(b)). Then, the droplet rear forms a curvature at the entrance of the bifurcation bulging in the upstream direction. In this

process a neck forms in the central part of the junction with a width decreasing in time (see Figure 4.1(c)). This behavior is presumably due to the flow of the carrier phase which actually flattens the dispersed phase against the sidewall of the bifurcation. As the circumference of the thread becomes less than its normal length, the surface tension starts to contract it radially promoting the incipience and growth of an instability similar to the Rayleigh-Plateau (see Section §2.6). This eventually results in a pinch-off and the formation of two almost equally sized daughter droplets that propagate downstream in the channel branches (see Figure 4.1(d)).

4.1.2 Non-breakup regime

By reducing the Ca number, in comparison with the preceeding case, cohesion forces become more relevant (see section 2.2), and thus we observe a radically different droplet behavior as reported in Figure 4.2 for a system with halved velocity u_c compared to the previous one. Here, initially, the droplet reduces its speed and approaches the junction in a similar fashion as reported above (see Figure 4.2(a)). However, now, the dominating surface tension force reduces the ability of the inertia and viscous force to deform the droplet which obtains a quasi steady-state condition, with no internal flow, as it sticks in the junction. Due to the stronger interfacial force, a larger curvature is generated at the droplet rear, resulting in a larger radius of the liquid thread (see Figure 4.2(b)). This has a direct consequence on the resulting droplet dynamics, as the birth of a Rayleigh-Plateau instability is prevented. The incipience of a random disturbance, generates a slightly asymmetric flow in the film formed between the droplet interface and the channel surface opening a tunnel on one side of the junction (see Figure 4.2(c)). As this perturbation grows, the droplet starts steering in the opposite arm (see Figure 4.2(d)) and eventually migrates entirely in this direction (see Figure 4.2(e)). This leaves an asymmetric distribution of the phases in the daughter branches and the droplet wrapping generates a continuous phase's flow recirculation in the other arm.

A mathematical formalization of the physical phenomena involved in breakup and non-breakup regimes has been proposed in a recent paper by Leshansky and Pismen[14]. Indeed, they developed an analytical theory that describes the
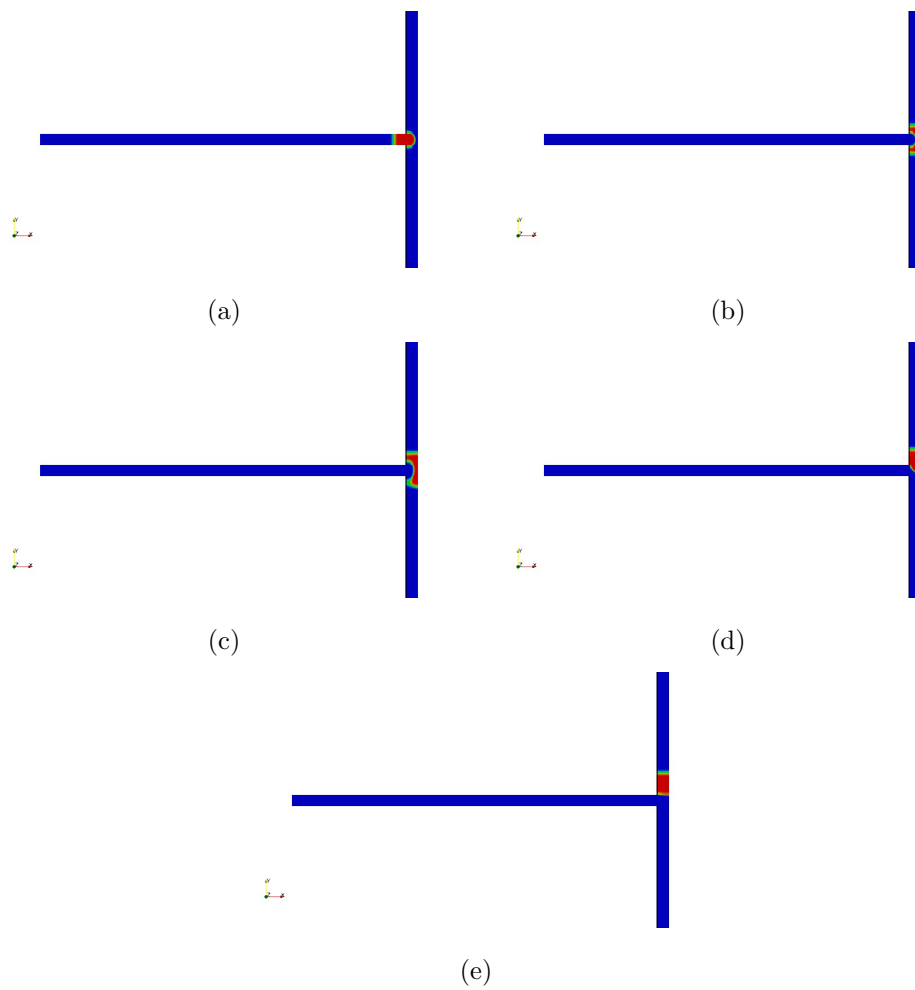
(a)

(b)

(c)

(d)

(e)

Figure 4.2: Typical droplet dynamics in non-breakup regime at the bifurcation.

breakup process in a symmetric two-dimensional T-junction driven by the observation of the pressure evolution in the droplet at the bifurcation. Although this analysis works in a limited 2D setting, the formula derived by Leshansky and Pismen agrees well with both 2D and 3D simulations and experimental findings from literature[15].

In particular, they could determine the conditions under which stationary solutions exist. This range corresponds, physically, to non-breakup case that is, as already stated, the case we are interested in. On this purpose, the boundary between non-breakup and breakup regions is given by the following important formula (continuous line in Figure 4.3):

$$\frac{L_d}{w} \approx \chi Ca^{-0.21} \tag{4.1}$$

where L_d [m] is the length of the droplet that approaches the T-junction, w [m] is the width of the channels, Ca is the Capillary number (see Section §2.2) and χ is a dimensionless parameter that depends on the ratio between the viscosities of dispersed and continuous phase $\lambda = \frac{\mu_d}{\mu_c}$: experimental evidences[11] demonstrate that the fitting χ decreases as λ increases. It can be noted that, once we fix λ, the transition between non-breakup and breakup regions is ruled only by two parameters: Ca and L_d (w is, in fact, a fixed geometrical parameter of the microfluidic system). In details, if we consider L_d as a constant, lower Capillary numbers lead to a wider non-breakup region. This behavior can be intuitively explained by ascertaining that small Capillary numbers mean that interfacial tension force dominates viscous force and thus it correspond to a situation of big cohesion between droplet's molecules.

On the other side, if we fix Ca, the greater is the droplet's length, the lower the corresponding non-breakup region. In turn, this phenomenon finds the following intuitive explanation: the least energy configuration for a droplet corresponds to the spherical geometry. Now, since physical systems tend intrinsically to move to the minimum energy state, breakup will affect more easily the most elongated drops (which are also the most energetic ones) in order to take them back to a spherical shape.

4.1.3 Simulations and numerical results

In order to validate the theoretical background presented, we carried out a series of simulations in symmetric 3D T-junctions using the finite volume based open-source code OpenFOAM (see Appendix A). The breakup has been simulated in a confined T-junction with uniform channels' width $w = 150\mu m$ and height $h = 50\mu m$ at varying Capillary numbers $Ca = \frac{\mu_c u_c}{\sigma}$ and different initial length L_d of the parent droplet. Our simulations almost successfully capture the transition between breaking and non-breaking regimes. It is shown (Figure 4.3) that if Capillary number is smaller than a critical number given by Equation (4.1), the droplet will move either to the left or right instead of breaking into two daughter droplets. Moreover, the critical Capillary number decreases with increasing droplet length. The χ parameter of Equation (4.1) considered in the theoretical curve of Figure 4.3 is equal to 0.187.
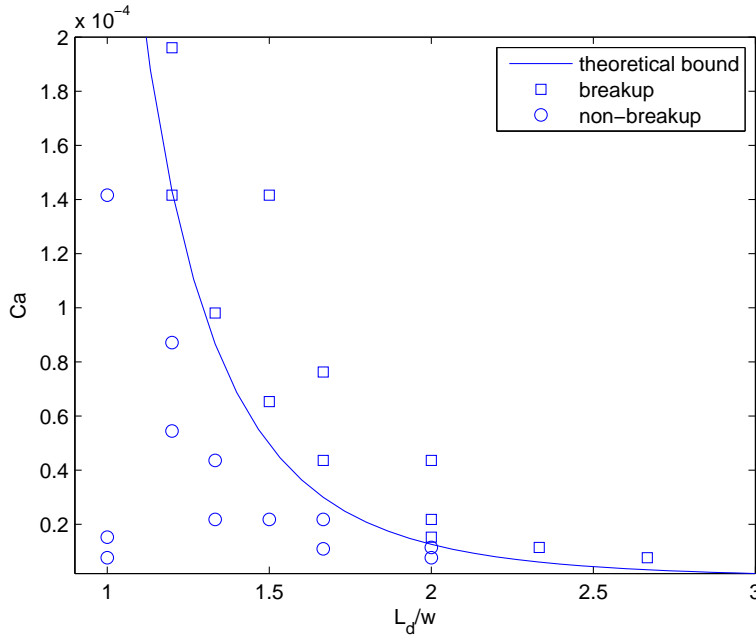

Figure 4.3: Phase diagram of numerical simulations for a drop in a symmetric T-junction. The solid line is the theoretical curve given by Equation (4.1) for $\chi = 0.187$. The symbols correspond to numerical results for nonbreaking ($\circ$) and breaking ($\square$) drops.

4.2 Regulation of droplet traffic in a T-junction

The next logical step we need to deal with, is the definition of a method to precisely carry the non-splitting droplets in the desired arm of the T-junction. The solution to this problem is provided by a simple property of microfluidic droplet systems[16, 17] at a T-junction (neglecting splitting, direct interactions and collisions) an arriving droplet follows the instantaneously leading flow rate. So, if the total original flow rate Q of the parent channel divides between Q_1 and $Q_2 = Q - Q_1$ in the two daughter branches (see Figure 4.4(a)), the sign of $Q_1 - Q_2$ decides in which arm the arriving droplet goes. More precisely, if $Q_1 > Q_2$ the choice falls on the daughter channel number 1 and vice versa.

Accordingly, if we manage to create an asymmetry in the flows of the two arms of a bifurcation, we are able to predict exactly the direction of the coming droplets. In order to do this, let's start noting that the T-junction depicted in Figure 4.4(a) corresponds, thanks to the electric circuit analogy (see Section §2.7), to the parallel resistance reported in Figure 4.4(b).
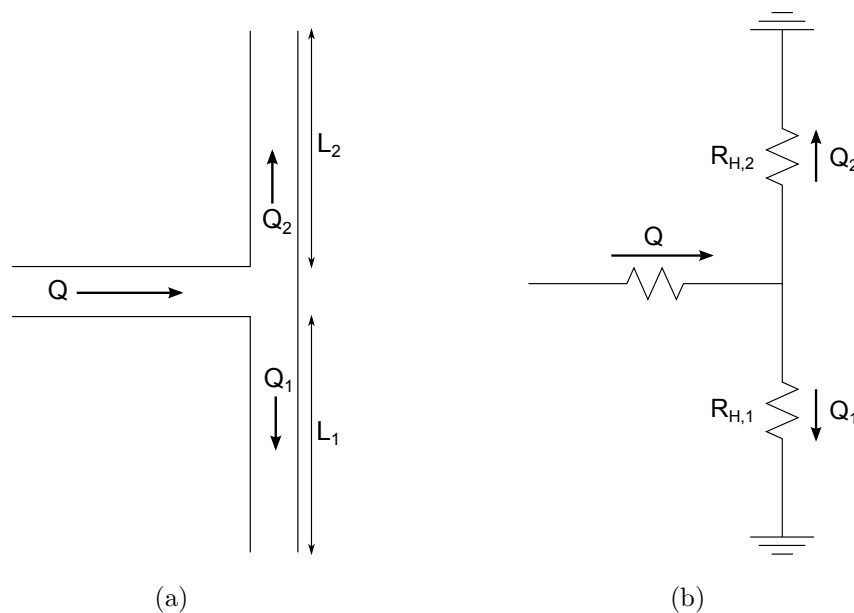

Figure 4.4: (a) Microfluidic symmetric T-junction and (b) its analogous electric circuit.

Moreover, we remember the concept of hydraulic resistance of a generical microfluidic channel introduced in Section §2.7, which is given by:

$$R_{H,i} = \frac{a\mu_c L_i}{wh^3} \tag{4.2}$$

where $\mu_c[Pa \cdot s]$ is the dynamic viscosity of the flowing liquid, $L_i[m]$ is the length of the channel, $w[m]$ is the width of the channel, $h[m]$ is the height of the channel and a is a dimensionless parameter defined as $a = 12[1 - \frac{192h}{\pi^5 w}tanh(\frac{\pi w}{2h})]^{-1}$.

Premising that w, h and consequently a are normally identical for the two arms of a T-junction, we can opportunely change L_1 and L_2[1] (see Figure 4.5(a)) in order to obtain $R_{H,1} \neq R_{H,2}$. In particular, $L_1 > L_2 \Rightarrow R_{H,1} > R_{H,2}$. In this way, we are able to achieve the desired initial unbalance between Q_1 and Q_2 that can be calculated using the current division law (see Section §2.7):

$$Q_1 = \frac{R_{H,2}}{R_{H,1} + R_{H,2}}Q \qquad Q_2 = \frac{R_{H,1}}{R_{H,1} + R_{H,2}}Q \qquad (4.3)$$

Therefore, relying on the previous equation, the arm with the leading flow rate Q_i in the bifurcation is the one with lower hydraulic resistance $R_{H,i}$ (channel 1 in figure Figure 4.5(a)) and the choice of the incoming non-splitting droplet will fall on this one (see Figure 4.5(b)).

The last aspect left to evaluate concerns the analysis of the effects induced by the presence of a droplet in one arm of the bifurcation. As we already pointed out in the non-breaking regime description, flows involving non-splitting droplets are inherently asymmetric since the presence of the latter in one arm of the T-junction increases the volumetric flow rate of the opposite channel. In this way, droplets act as a series flow resistance in the branch they occupy.

In order to quantify the additional resistance involved by droplets, we should notice that their presence in a channel change the dynamic viscosity μ_d of the portion L_d they occupy. Thus, referring to Equation (2.21), the hydraulic resistance ascribable to the droplet is given by:

$$R_{H,d} = \frac{\mu_d L_d a}{wh^3} \qquad (4.4)$$

Then, the new resistance $(R'_{H,i})$ of the channel, can be obtained by summing $R_{H,d}$ to the original hydraulic resistance $(R_{H,i})$ of the same and subtracting the quantity $\frac{\mu_c L_d a}{wh^3}$ (this is due to the fact that the original $R_{H,i}$ considered a channel completely filled by continuous phase which is not true anymore for the portion

---

[1]For the moment, we exclude the presence of any droplets in the bifurcation, so $\mu_1 = \mu_2 = \mu_c$, because we are interested in the behavior of the first drop that approach the T-junction. The opposite case is discussed later.

L_d occupied by the droplet). So, we can rewrite $R'_{H,i}$ as follows:

$$R'_{H,i} = R_{H,i} + \delta r = \frac{a\mu_c L_i}{wh^3} + (\mu_d - \mu_c)\frac{L_d a}{wh^3} \qquad (4.5)$$

where $\delta r = (\mu_d - \mu_c)\frac{L_d a}{wh^3}$ is the additional resistance per droplet.

Accordingly, in the case of Figure 4.5(b), the current division law returns:

$$Q'_1 = \frac{R_{H,2}}{R_{H,1} + \delta r + R_{H,2}}Q \qquad Q'_2 = \frac{R_{H,1} + \delta r}{R_{H,1} + \delta r + R_{H,2}}Q \qquad (4.6)$$

Finally, two different cases may occur:

- if Q'_1 is still greater than Q'_2 in Figure 4.5(b), the next coming droplet will select, in turn, channel number 1 in the bifurcation (see Figure 4.5(c));

- if δr is great enough to invert the channel with the leading flow rate ($Q'_2 > Q'_1$ in Figure 4.5(b)), the next coming droplet will select branch 2 differently from the first bubble's choice (see Figure 4.5(d)).

From this examination, we can appreciate how the droplet sorting problem is intrinsically non linear and complex. The hydrodynamic resistance of each arm of the bifurcation depends, in fact, both from its geometrical properties and from the number and size of the droplets it contains. Consequently, the instantaneous "choice" of the droplets depends on the past hystory of the flow. Such a nonlinear "memory kernel" renders the process very sensitive and complicates significantly its analysis.

4.2.1 Simulative example

In order to validate the model introduced for the droplet sorting problem, we ran several simulations using OpenFOAM, experiencing an almost perfect agreement with our theoretical solution.

On this purpose, Figure 4.6 represent a significant example. Here, we collect the results obtained from a simulation characterized by the following settings:

We can observe, in accordance with the theory, that the first droplet approaching the bifurcation (Figure 4.6(a)) turns to the right channel (lower channel in Figure 4.6(b)): this branch, in fact, is shorter than the other one and has, consequently, the lowest initial hydraulic resistance (see Equation (4.2)):

$$\begin{aligned} R_{H,1} &= \tfrac{a\mu_c L_1}{wh^3} \approx 1.62 \cdot 10^{12} Pa \cdot s/m^3 \\ R_{H,2} &= \tfrac{a\mu_c L_2}{wh^3} \approx 4.05 \cdot 10^{12} Pa \cdot s/m^3 \end{aligned} \qquad (4.7)$$
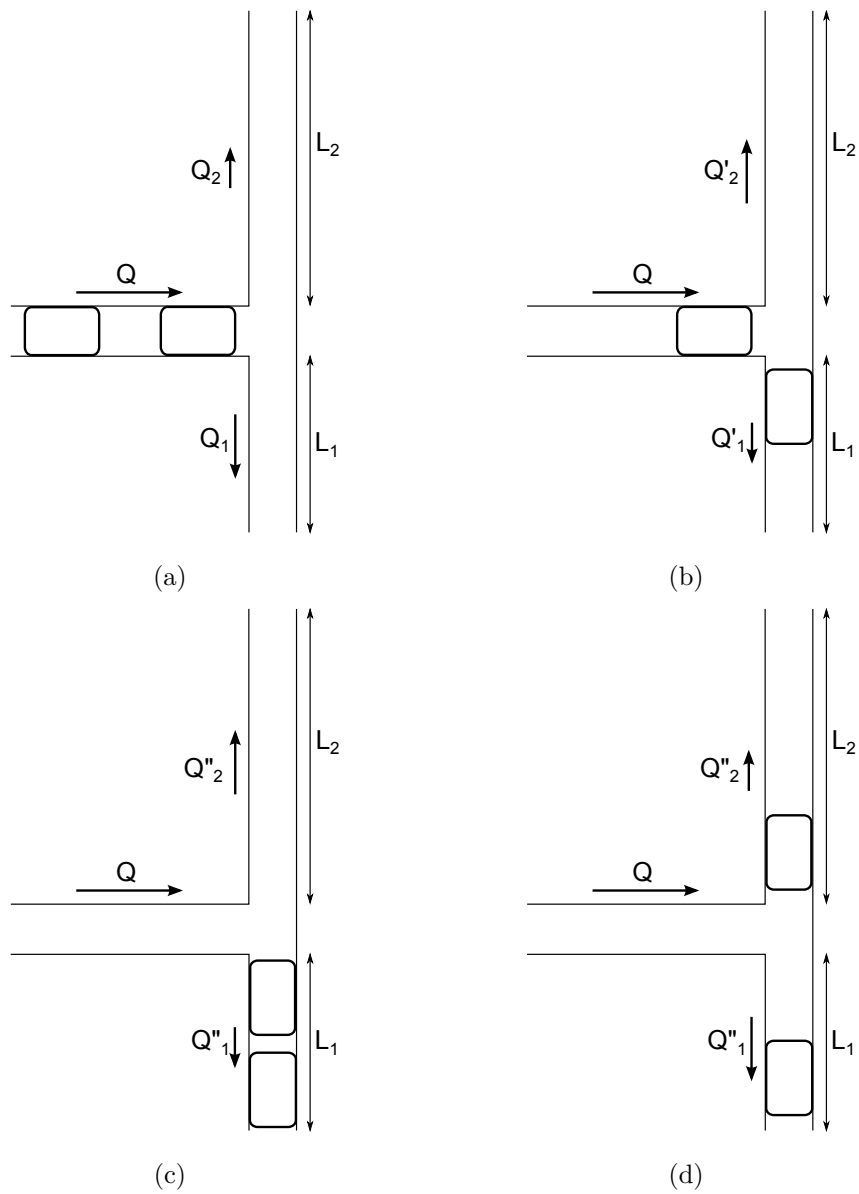
Figure 4.5: Example of droplet sorting problem.

Simulation settings	
Dispersed phase viscosity	$\mu_d = 145.5\ mPa \cdot s$
Continuous phase viscosity	$\mu_c = 1.002\ mPa \cdot s$
Droplets' length	$L_{d_1} = L_{d_2} = 200\ \mu m$
Channels' width	$w = 150\ \mu m$
Channels' height	$h = 50\ \mu m$
First branch's length	$L_1 = 2mm$
Second branch's length	$L_2 = 5mm$
Input volumetric flow rate	$Q = 2.625nL/s$

Table 4.1: Geometrical and physical properties of the reference system

and thus the leading flow rate (see Equation (4.3)):

$$Q_1 = \frac{R_{H,2}}{R_{H,1}+R_{H,2}}Q \approx 1.88nL/s$$
$$Q_2 = \frac{R_{H,1}}{R_{H,1}+R_{H,2}}Q \approx 0.75nL/s$$

(4.8)

Immediately, the presence of the droplet in the right arm, increases its resistance in accordance with Equation (4.5):

$$R'_{H,1} = R_{H,1} + \delta r_1 = \frac{a\mu_c L_1}{wh^3} + (\mu_d - \mu_c)\frac{L_{d_1}a}{wh^3} \approx 2.50 \cdot 10^{13}Pa \cdot s/m^3$$
$$R'_{H,2} = R_{H,2} = \frac{a\mu_c L_2}{wh^3} \approx 4.05 \cdot 10^{12}Pa \cdot s/m^3$$

(4.9)

This additional resistance is great enough to make $Q'_2 > Q'_1$:

$$Q'_1 = \frac{R'_{H,2}}{R'_{H,1}+R'_{H,2}}Q \approx 0.37nL/s$$
$$Q'_2 = \frac{R'_{H,1}}{R'_{H,1}+R'_{H,2}}Q \approx 2.26nL/s$$

(4.10)

and, thus, the next coming droplet will move, contrary to the previous case, to the left channel (upper channel in Figure 4.6(c)).

Our idea is to exploit this physical behavior to direct the droplets in our microfluidic network as illustrated in the next chapter.

In conclusion, it is important to note that our theoretical model predicts an increase in the hydraulic resistance of the channel caused by the presence of a droplet if and only if $\mu_d > \mu_c$ (in accordance with Equation (4.5)). This phenomenon can be explained remembering that viscosity (see Section §2.1) describes the fluid's internal resistance to flow: the greater the viscosity, the greater its resistance to flow and vice versa.
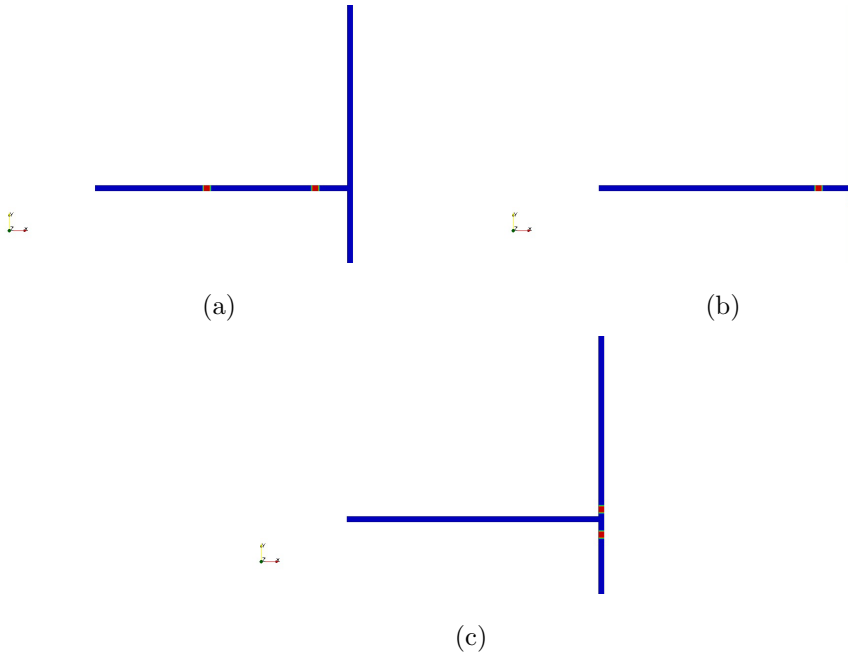
Figure 4.6: Simulation of droplet sorting problem.

So, if droplets have a characteristic dynamic viscosity $\mu_d > \mu_c$ we, effectively, inject in the microfluidic system a substance that opposes strongly to the motion and ultimately increases the resistivity of the channel it occupies (the term δr in Equation (4.5) is positive). Otherwise, if $\mu_d < \mu_c$, we inject a mobile liquid which decreases the hydraulic resistance of the carrier channel (the term δr in Equation (4.5) becomes negative).

This dynamic is consistent with the simulations we obtained with OpenFOAM though some experiments from research groups prove that there is an increase in channel resistance even if we inject a dispersed phase having $\mu_d < \mu_c$. On this purpose, we suppose that the lack of the occurrance of this behavior in our simulations is imputable to the limitations of the solver used (see Appendix A). Most likely, in fact, it isn't able to capture the friction's sources different from viscous force (e.g., the pressure exerted to the droplet by the thin films of continuous phase that wrap the dispersed fluid).

Consequently, the model proposed may fail for situations in which viscous forces are not the dominant friction contribution and thus it is mainly applicable when $\mu_d \gg \mu_c$.

Chapter 5

Design and performance of a microfluidic bus network

As anticipated, our aim is to create a programmable LoC in which several elements (microfluidic machines), able to perform specific laboratory functions, are deployed in a single "unit" and connected together to form a network. Accordingly, it is possible to support different complex laboratory processes in the same chip simultaneously, which has several advantages: cost of LoCs could be reduced, their reusability could be increased and their effectiveness could be improved by supporting higher flexibility and time saving.

A crucial step in this direction is the identification of an appropriate approach to transmit "packets" (droplets) to the "end users" (microfluidic machines) of the microfluidic network. In this chapter we'll analyze a promising solution to this problem and discuss the performance obtained for a microfluidic network with bus topology.

5.1 Mechanism for droplet routing

First of all, let's then consider a microfluidic bus network topology as depicted in Figure 5.1, where N is the number of microfluidic machines (MM) connected. Physically, it simply consists of a main "transmission channel" ramified several times in order to reach all the microfluidic machines. Let's note that, for the sake of simplicity, we considered a uniform spacing (L) between the various branches. In such configuration, a drop destined to the i-th MM is injected into the network

51

through a generator (see Section §3.3) placed at the "input port" on the left, cross the main channel until it's finally diverted in the i-th target branch.
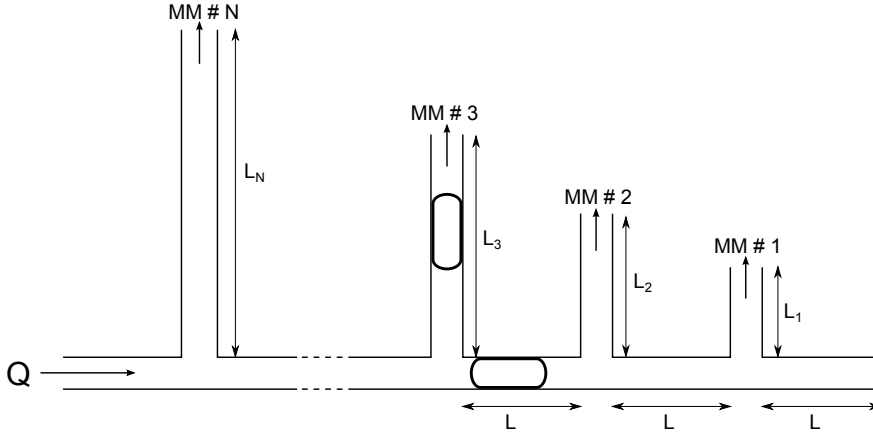

Figure 5.1: Design of a microfluidic network with bus topology.

Once again, in order to fully understand the mechanism we developed for routing the drops, comes in handy the fluidic/electric parallelism (see Section §2.7). Accordingly, in Figure 5.2 we reported the electric circuit that correspond to the fluidic network depicted in Figure 5.1 where R is the hydraulic resistance due to the linking stretches of length L, R_n is the characteristic resistance of the n-th branch and $R_{eq,n}$ is the equivalent resistance seen downstream of the n-th branch in case of droplets' absence. Another important premise, that will be understood later on, is to impose the common main channel to be the path with the starting leading flow.
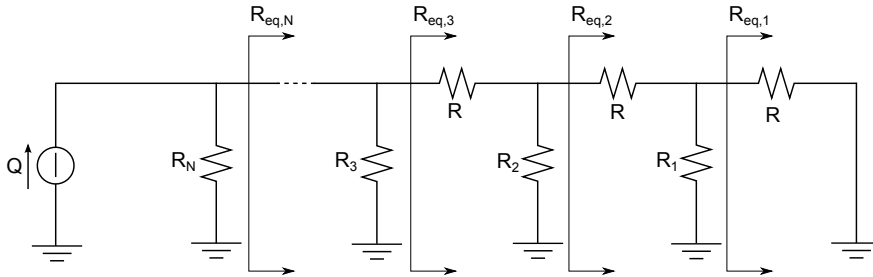

Figure 5.2: Electric circuit analogous to the microfluidic bus network.

Suppose, now, that we want to bring a droplet cargo with a certain volume at the i-th MM. Our solution to fulfill this goal requires the injection of two very close droplets in the system: a "header droplet" and a "payload droplet". As already

discussed, the first one (hereafter header droplet) will always follow the path with the original leading flow, i.e. the main microchannel, due to the hypothesis just made. Furthermore, it will increment, time after time, the resistance of the duct it occupies in accordance with Equation (4.5). This physical behavior may allow us to deflect the following droplet in the desired target branch. Let's, in fact, focus on the generic i-th bifurcation which is constituted by two parallel arms with characteristic original hydraulic resistances respectively equal to R_i and $R_{eq,i} = R + R_{i-1} \parallel R_{eq,i-1}$ (see Figure 5.2). The presence of the header droplet in the portion connecting ramification i and $i-1$ will change $R_{eq,i}$ as follows:

$$R'_{eq,i} = R + \delta r_i + R_{i-1} \parallel R_{eq,i-1} \tag{5.1}$$

where $\delta r_i = \frac{(\mu_d - \mu_c) a L_{d_i}}{w h^3}$ is the resistance increment due to the header droplet[1]. If δr_i is large enough to reverse the leading flow arm at the i-th bifurcation, the second drop (hereafter payload droplet) won't flow anymore in the main channel but it will rather enter in the i-th branch reaching the desired target microfluidic machine. The header droplet, in turn, continues along the main channel and it's eventually discarded from the system via the output port on the right (see Figure 5.1): this droplet, in fact, doesn't carry "useful fluid" but it rather serves only to divert the actual payload droplet to the correct destination.

So far, we have given a qualitative description of the routing process we developed. Now, however, we have to mathematically formalize it in order to correctly model the microfluidic network of Figure 5.1.

5.2   Bus network dimensioning

First of all, we have seen that the header droplet must always flow along the whole main channel without being deflected at any ramifications. Only in this way, in fact, it may opportunely affect the payload droplets' route deviating them in the correct branch. This requirement translates, ultimately, in the following

---

[1]Note that we implicitly impose that the header droplet is in the channel connecting ramification i and $i-1$ when the payload droplet approaches the i-th bifurcation because we assume that they are injected very closely to each other.

condition:

$$R_n > R_{eq,n}, \ \forall n = 1, ..., N \tag{5.2}$$

where R_n is the characteristic hydraulic resistance of the n-th branch and $R_{eq,n}$ is the equivalent parallel resistance seen downstream of the n-th branch in case of droplet's absence. Equation (5.2) can be rewritten by observing that the circuit configuration of Figure 5.2 has an intrinsic redundancy. Indeed, the following recursive pattern can be identified:

$$R_{eq,n} = R + R_{n-1} \parallel R_{eq,n-1}, \ \forall n = 1, ..., N \tag{5.3}$$

with $R_{eq,1} = R$ (or equivalently $R_{eq,0} = 0$). This logical step allows us to calculate $R_{eq,n}$ as a function of $R_{eq,n-1}$. Substituting it in Equation (5.2), in fact, we obtain:

$$R_n > R + R_{n-1} \parallel R_{eq,n-1}, \ \forall n = 1, ..., N \tag{5.4}$$

This condition imposes, therefore, a lower bound to the various R_n which, consequently, can be calculated as follows:

$$R_n = \alpha R_{eq,n} = \alpha(R + R_{n-1} \parallel R_{eq,n-1}), \ \forall n = 1, ..., N \tag{5.5}$$

with α being a dimensionless discretionary parameter strictly greater than 1 ($\alpha > 1$).

Now, we need to establish the correct resistance increment δr_i caused by a header droplet in order to deflect the cargo in a generic i-th branch of the network. Thus, we have to impose two different conditions:

1. The payload droplet must select the branch containing the i-th microfluidic machine when it arrives at the corresponding bifurcation. Mathematically, it consists in having $R'_{eq,i} = R + \delta r_i + R_{i-1} \parallel R_{eq,i-1} > R_i$, where $R'_{eq,i}$ is the equivalent resistance seen downstream of the i-th branch in case of i-th header droplet's presence. Consequently, $\delta r_i > R_i - R_{eq,i} = R_i - (R + R_{i-1} \parallel R_{eq,i-1})$.

2. Moreover, we must ensure that the payload droplet doesn't enter into any of the outreaches it encounters before the i-th bifurcation, which means that: $R'_{eq,k} = R + \delta r_i + R_{k-1} \parallel R_{eq,k-1} < R_k, \ \forall k = i+1, ..., N$. It can be demonstrated that condition necessary and sufficient to satisfy this requirement

is: $R'_{eq,i+1} = R + \delta r_i + R_i \parallel R_{eq,i} < R_{i+1}$. Therefore, $\delta r_i < R_{i+1} - R_{eq,i+1} = R_{i+1} - (R + R_i \parallel R_{eq,i})$

Generalizing the previous reasoning, we obtain both a lower and an upper bound for the various δr_n, $\forall n = 1, ..., N$ (i.e. the resistance increments that a header must entail in order to route the following payload droplet to the various n-th microfluidic machine of the bus network). In particular, condition number 1. implies:

$$\delta r_n > R_n - R_{eq,n}, \ \forall n = 1, ..., N \tag{5.6}$$

whereas, condition number 2. entails:

$$\delta r_n < R_{n+1} - R_{eq,n+1}, \ \forall n = 1, ..., N \tag{5.7}$$

Furthermore, substituting Equation (5.3) in Equations (5.6) and (5.7), we obtain, respectively:

$$\delta r_n > R_n - (R + R_{n-1} \parallel R_{eq,n-1}), \ \forall n = 1, ..., N \tag{5.8}$$

$$\delta r_n < R_{n+1} - (R + R_n \parallel R_{eq,n}), \ \forall n = 1, ..., N \tag{5.9}$$

Finally, δr_n can be calculated as follows:

$$\delta r_n = \beta(R_{n+1} - R_{eq,n+1}) + (1 - \beta)(R_n - R_{eq,n}), \ \forall n = 1, ..., N \tag{5.10}$$

with β being a dimensionless discretionary parameter between 0 and 1 ($0 < \beta < 1$). For the sake of simplicity, we chose the convention to take the mean value between lower and upper bound thus always considering $\beta = 0.5$.

Let's now remember (see Section §4.2) that δr_n is linked to the geometrical and physical parameters of the system in accordance with the following formula:

$$\delta r_n = \frac{(\mu_d - \mu_c)aL_{d_n}}{wh^3} \tag{5.11}$$

where μ_d is the viscosity of the header droplet, μ_c is the viscosity of the continuous phase, w is the width of the channels, h is the height of the channels, a is a geometrical parameter which depends on the ratio w/h and L_{d_n} is the length of the header droplet.

If we consider that μ_d, μ_c, w and h are normally fixed, the only parameter we can change, in order to vary δr_n, is L_{d_n}. So, we can create a header droplet able to divert the payload exactly at the desired ramification just by modulating opportunely its length L_{d_n}. Nonetheless, if we want the model introduced above to work correctly, we need to respect a series of mathematical and physical constraints that are the topic of the next Section.

5.2.1 Mathematical and physical constraints

First of all, it is important to note that the two formulas in Equations (5.8) and (5.9) impose us to respect a very precise mathematical constraint. The lower bound, in fact, must always be smaller than the upper bound otherwise the problem won't have solution:

$$R_n - R_{eq,n} < R_{n+1} - R_{eq,n+1}, \ \forall n = 1, ..., N \tag{5.12}$$

Substituting Equation (5.5), we obtain:

$$R_n \left(1 - \frac{1}{\alpha}\right) < R_{n+1} \left(1 - \frac{1}{\alpha}\right) \Rightarrow R_n < R_{n+1}, \ \forall n = 1, ..., N \tag{5.13}$$

A transversal result deductible from Equation (5.13) is that $L_1 < L_2 < ... < L_N$. In fact, if we retrieve the concept of hydraulic resistance (see Equation (4.2)), we can express R_n as $\frac{a\mu_c L_n}{wh^3}$. Then, Equation (5.13) becomes:

$$\frac{a\mu_c L_n}{wh^3} < \frac{a\mu_c L_{n+1}}{wh^3} \Rightarrow L_n < L_{n+1}, \ \forall n = 1, ..., N \tag{5.14}$$

leading us to the anticipated result (indeed, it is no concidence that in Figure 5.1 we placed the branches, from left to right, in rigorous decreasing order of length).

After this dutiful parenthesis, we shall continue our analysis expliciting Equation (5.13). In particular, availing of Equation (5.5), we obtain:

$$R_n < \alpha(R + R_n \parallel R_{eq,n}), \ \forall n = 1, ..., N \tag{5.15}$$

and, applying the well-known rule for parallel resistance:

$$R_n < \alpha(R + \frac{R_n R_{eq,n}}{R_n + R_{eq,n}}) = \alpha R + \alpha \frac{R_n \frac{R_n}{\alpha}}{R_n + \frac{R_n}{\alpha}} = $$
$$= \alpha R + \frac{\alpha}{1+\alpha} R_n, \ \forall n = 1, ..., N \tag{5.16}$$

Moreover, simplifying and inverting Equation (5.16), it results:

$$R > \frac{R_n}{\alpha(1 + \alpha)}, \ \forall n = 1, ..., N \tag{5.17}$$

Of course, we are writing the same thing if we substitute the previous equation with:

$$R > \frac{max\{R_n\}}{\alpha(1 + \alpha)} \tag{5.18}$$

and, reminding Equation (5.13), we can also infer that $max\{R_n\} = R_N$. So, Equation (5.18) becomes:

$$R > \frac{R_N}{\alpha(1+\alpha)} \tag{5.19}$$

However, in this formula, we still have to render explicit R_N which we know to be, in turn, a function of R and α.

In order to get it, we may exploit the intrinsic redundancy of the system. Let's, in fact, start calculating R_1. Taking advantage of Equation (5.5), it simply results:

$$R_1 = \alpha R \tag{5.20}$$

For the same reason, we obtain:

$$R_2 = \alpha(R + R_1 \parallel R_{eq,1}) = \alpha(R + \alpha R \parallel R) = \frac{\alpha R}{1+\alpha}[(1+\alpha)+\alpha] \tag{5.21}$$

$$R_3 = \alpha(R + R_2 \parallel R_{eq,2}) = \frac{\alpha R}{(1+\alpha)^2}\{(1+\alpha)^2 + \alpha[(1+\alpha)+\alpha]\} \tag{5.22}$$

and so on.

The way we wrote the results highlights the common pattern recognizable at the basis of the previous formulas. In particular we can express a generic R_i as:

$$R_i = \frac{\alpha R}{(1+\alpha)^{i-1}}[(1+\alpha)^{i-1} + \alpha(1+\alpha)^{i-2} + ... + \alpha^{i-2}(1+\alpha) + \alpha^{i-1}] \tag{5.23}$$

Furthermore, we can compact the notation in Equation (5.23) by means of the following summation:

$$R_i = \frac{\alpha R}{(1+\alpha)^{i-1}} \sum_{k=1}^{i} \alpha^{k-1}(1+\alpha)^{i-k} \tag{5.24}$$

Finally, we are now able to calculate the desired resistance R_N as:

$$R_N = \frac{\alpha R}{(1+\alpha)^{N-1}} \sum_{k=1}^{N} \alpha^{k-1}(1+\alpha)^{N-k} \tag{5.25}$$

Substituting this important result in Equation (5.19), we gather:

$$R > \frac{\frac{\alpha R}{(1+\alpha)^{N-1}} \sum_{k=1}^{N} \alpha^{k-1}(1+\alpha)^{N-k}}{\alpha(1+\alpha)} = \frac{R}{(1+\alpha)^N} \sum_{k=1}^{N} \alpha^{k-1}(1+\alpha)^{N-k} \tag{5.26}$$

Thus, lastly, by simplifying the above formula, we obtain a constraint that depends solely by the parameter α and the number of microfluidic machine N in the system:

$$\frac{\sum_{k=1}^{N} \alpha^{k-1}(1+\alpha)^{N-k}}{(1+\alpha)^N} < 1 \tag{5.27}$$

For the sake of simplicity, hereafter we'll indicate the quantity $\frac{\sum_{k=1}^{N} \alpha^{k-1}(1+\alpha)^{N-k}}{(1+\alpha)^N}$ with $C_1(\alpha, N)$ so, the previous equation becomes:

$$C_1(\alpha, N) < 1 \tag{5.28}$$

As we see in the next graph (Figure 5.3), this condition is always satisfied for any $\alpha > 1$ and N. However, if C_1 is nearly equal to 1, it means that the lower bound for δr_n (see Equation 5.8) is almost identical to its upper bound (see Equation 5.9) and thus the system is very unstable and strongly susceptible to "noise" due to fabrication or setting imperfections[2]. In order to improve its robustness we
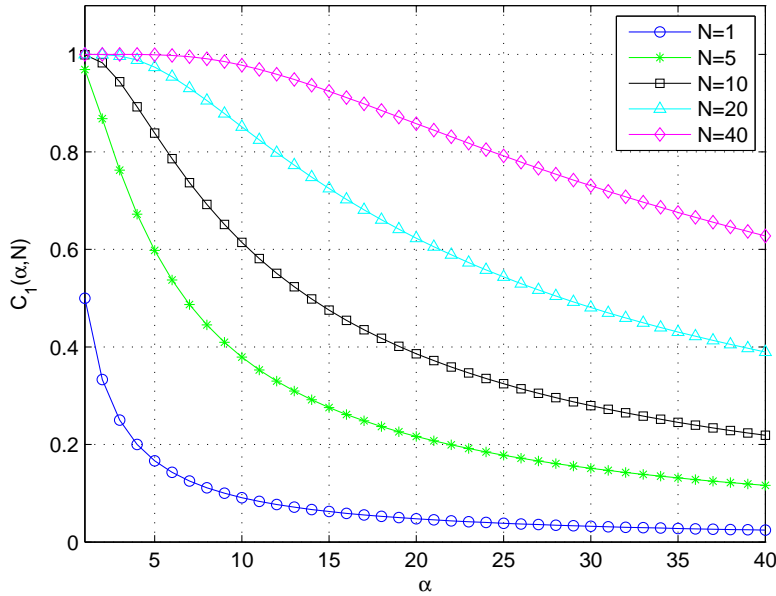

Figure 5.3: Trend of $C_1(\alpha, N)$ as a function of α for various N (number of microfluidic machines).

thus need to impose a certain margin on C_1 that cannot be too close to 1. Then, we have to strengthen the bond in Equation (5.28) by choosing a new threshold t_1 strictly less than 1:

$$C_1(\alpha, N) < t_1 \tag{5.29}$$

For example, if we fix $t_1 = 0.9$, it means that in Figure 5.3 we are interested in the portion of the curves located below $t_1 = 0.9$. Essentially, this implies that,

---

[2]This case occurs for for small values of α as N increases.

for increasing values of N we are forced to select higher values of α in order to respect the condition above.

This result is visually represented in Figure 5.4 where we plot, for various t_1, the curve which represents the minimum value that α can assume in order to satisfy Equation (5.29) as a function of N.
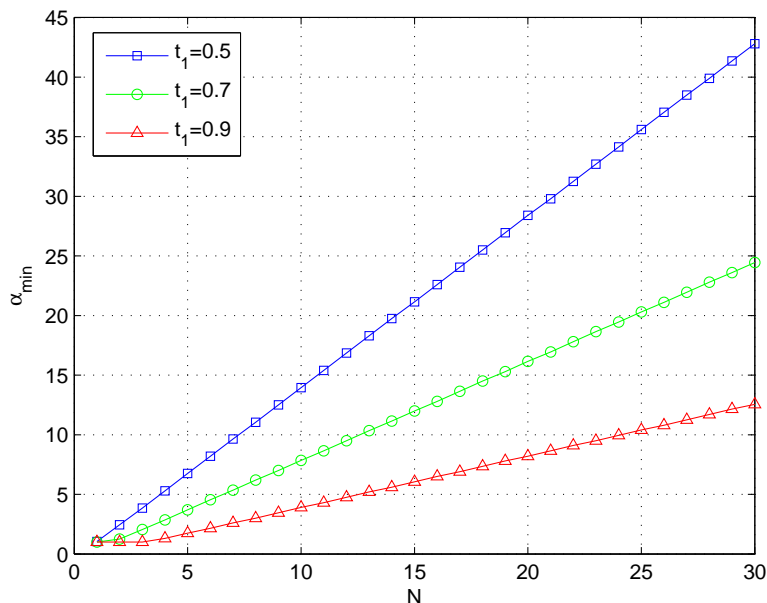

Figure 5.4: Minimum value of α imposed by Equation (5.29) as a function of N for various thresholds t_1.

Another very important constraint, of physical nature, that we need to respect concerns the fact that the header droplets must be entirely contained in the connecting channels between the branches otherwise it couldn't opportunely force the payload droplet to deviate towards the desired microfluidic machine. Only in this situation, in fact, the header droplet would increase the resistance of the duct it occupies in accordance with Equation (5.11). Therefore, the condition that we need to impose is:

$$L_{d_n} < L, \ \forall n = 1, ..., N \tag{5.30}$$

which coincides with:

$$max\{L_{d_n}\} < L \tag{5.31}$$

However, looking at Equation (5.11), we can deduce that the longest header drop is the one with the greatest δr_n, i.e. δr_N.[3] So, $max\{L_{d_n}\} = L_{d_N}$ and the previous formula turns into:

$$L_{d_N} < L \tag{5.32}$$

Furthermore, inverting Equations (5.11) and (2.21), and subtituting them in the formula above, we obtain:

$$\frac{\delta r_N w h^3}{(\mu_d - \mu_c)a} < \frac{R w h^3}{\mu_c a} \Rightarrow \delta r_N < \frac{(\mu_d - \mu_c)}{\mu_c} R \tag{5.33}$$

Now, exploiting Equation (5.10), it results:

$$\beta(R_{N+1} - R_{eq,N+1}) + (1 - \beta)(R_N - R_{eq,N}) < \frac{(\mu_d - \mu_c)}{\mu_c} R \tag{5.34}$$

that, thanks to Equation (5.5), corresponds to:

$$\beta(\alpha - 1)\left(R + \frac{1}{1 + \alpha} R_N\right) + (1 - \beta)R_N\left(\frac{\alpha - 1}{\alpha}\right) < \frac{(\mu_d - \mu_c)}{\mu_c} R \tag{5.35}$$

Then, after some basic math, we gain:

$$R > \frac{\alpha^2 - \beta\alpha + \beta - 1}{\alpha(\alpha + 1)\left[\frac{(\mu_d - \mu_c)}{\mu_c} + \beta(1 - \alpha)\right]} R_N \tag{5.36}$$

Now, again, we have to express R_N in explicit form as reported in Equation (5.25). So, we obtain:

$$R > \frac{\alpha^2 - \beta\alpha + \beta - 1}{\frac{(\mu_d - \mu_c)}{\mu_c} + \beta(1 - \alpha)} \frac{R}{(1 + \alpha)^N} \sum_{k=1}^{N} \alpha^{k-1}(1 + \alpha)^{N-k} \tag{5.37}$$

Dividing both sides by R, it finally results:

$$1 > \frac{\alpha^2 - \beta\alpha + \beta - 1}{\frac{(\mu_d - \mu_c)}{\mu_c} + \beta(1 - \alpha)} \frac{1}{(1 + \alpha)^N} \sum_{k=1}^{N} \alpha^{k-1}(1 + \alpha)^{N-k} \tag{5.38}$$

which is, once again, a condition that depends solely on α and N (in fact, we always consider a fixed $\beta = 0.5$ while μ_d and μ_c are physical parameters proper of the substances considered). Denoting the right member in Equation (5.38) with $C_2(\alpha, N)$, we can rewrite the formula above as:

$$C_2(\alpha, N) < 1 \tag{5.39}$$

---

[3]This is a consequence of Equations (5.8) and (5.9).

In Figure 5.5 we collected the results obtained for C_2 as a function of α and for various values of N. It can be noted that, contrary to C_1, the curves characterizing C_2 start from 0 and are monotonically increasing: consequently, for low α the condition above is largely satisfied while when α exceeds a critical maximum value the constraint isn't fullfilled anymore. Moreover, it results that, if N increases, this critical value decreases. Once again it is advisable to introduce a certain
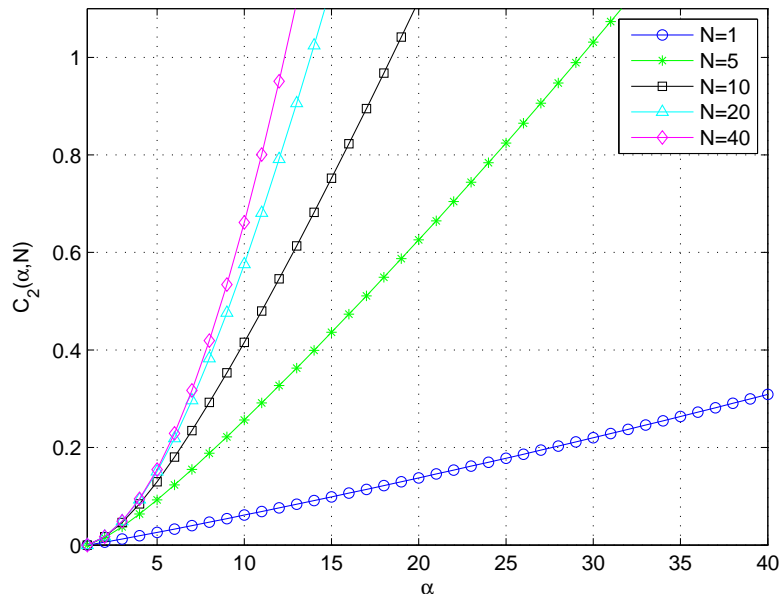

Figure 5.5: Trend of $C_2(\alpha, N)$ as a function of α for various N (number of microfluidic machines).

tolerance on the constraint of Equation (5.38) by imposing a threshold t_2 strictly lower than 1:

$$C_2(\alpha, N) < t_2 \tag{5.40}$$

In fact, if C_2 is nearly equal to 1, it means that the longest header droplet fits exactly the linking channel of length L leaving no margin and thus making the system unstable. Suppose now that we fix $t_2 = 0.9$. This choice involves that in Figure 5.5 we are interested in the portion of the curves located below $t_2 = 0.9$. Essentially, it implies that, for increasing values of N we'll have lower upper bound on α in order to respect the condition of Equation (5.40).

This reasoning is confirmed by looking at the graph in Figure 5.6 where we plot, for various t_2, the curve which represents the maximum value that α can
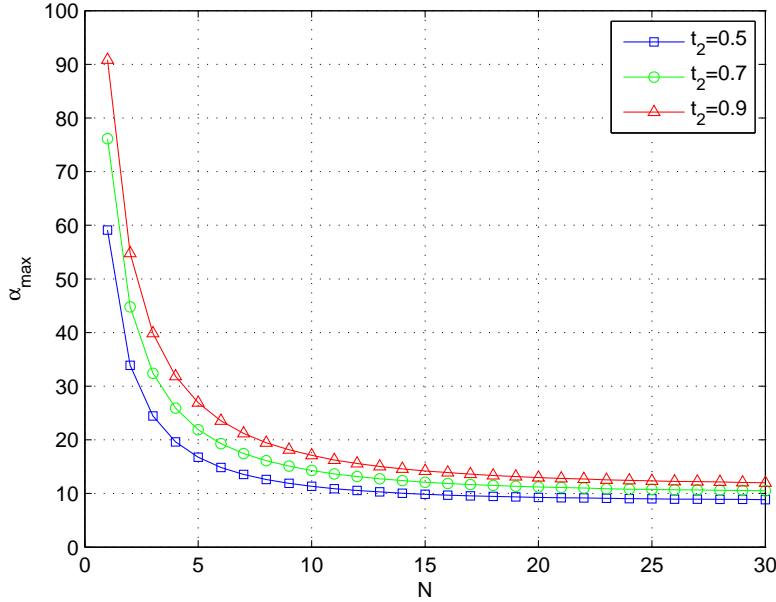
assume as a function of N.

Figure 5.6: Maximum value of α imposed by Equation (5.40) as a function of N for various thresholds t_2.

The two constraints analyzed so far are clearly in contraposition with each other: the former (Equation (5.29)), in fact, imposes a minimum α while the latter (Equation (5.40)) fixes a maximum value for the same prameter. In Figure 5.7 we report the graph obtained combining and processing both the curves in Figure 5.4 and in Figure 5.6.

The conclusions that can be drawn are that, fixing the thresholds t_1 and t_2,[4] there exists a specific region where the problem has solution (i.e., the area enclosed by the couples of curves with the same shape in Figure 5.7). Beyond this range no solution can be found. Consequently, the point where the two curves above intersect discriminates between the systems with solution and with no solution: α_{min}, in fact, must always stay under α_{max} in order to respect both constraints. Therefore, for N higher than the value of the abscissa where the two

---

[4]In our study we choose, for convenience, the same t_1 and t_2 though, obviously, they might be selected independently.
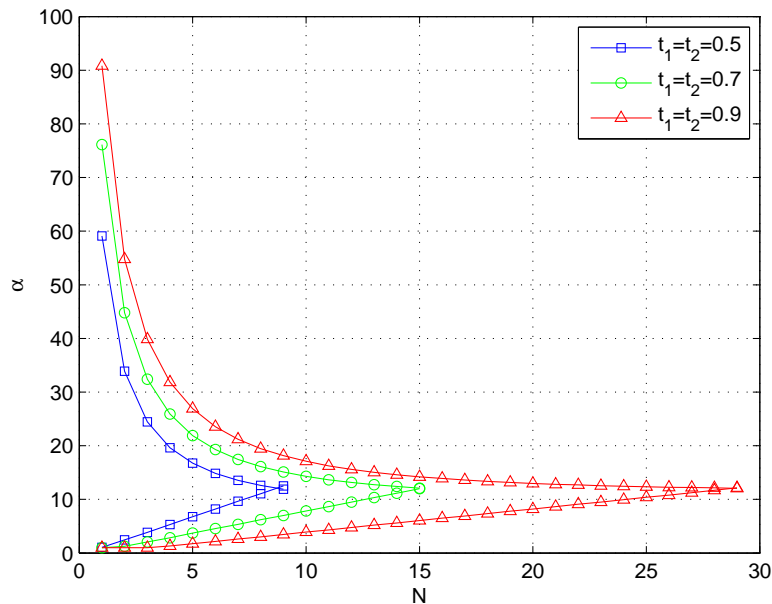
Figure 5.7: Minimum and maximum values of α imposed respectively by Equation (5.29) and (5.40) as a function of N for various thresholds $t_1 = t_2$.

curves cross each other, no solution can be found and, in such a situation, we may only proceed in two ways:

- we can choose a lower number of microfluidic machine N for our network, losing, however, in system scalability;

- we can loosen the bonds of Equations (5.29) and (5.40) selecting two new thresholds t_1 and t_2 greater than the previous ones. Accordingly, however, we'll lose in system robustness.

The last condition we have to satisfy in our model derives from the droplet generator we have chosen for our network. In fact, looking at the Equation (3.6), which defines the droplets length achievable by means of a cross-flowing generator in squeezing regime, it results that we cannot produce droplets shorter than w (with w being the width of the channels). This means that all the header droplets we consider need to be longer than w:

$$L_{d_n} > w, \ \forall n = 1, ..., N \tag{5.41}$$

which corresponds to impose:

$$min\{L_{d_n}\} > w \qquad (5.42)$$

We have already seen that $min\{L_{d_n}\} = L_{d_1}$, so, it becomes:

$$L_{d_1} > w \qquad (5.43)$$

Now, substituting Equation (5.11), we get:

$$\frac{\delta r_1 w h^3}{(\mu_d - \mu_c)a} > w \Rightarrow \delta r_1 > \frac{(\mu_d - \mu_c)a}{h^3} \qquad (5.44)$$

Remembering Equation (5.6), it results that condition necessary but not sufficient to satisfy this constraint is:

$$R_1 \left(1 - \frac{1}{\alpha}\right) > \frac{(\mu_d - \mu_c)a}{h^3} \qquad (5.45)$$

Finally, exploiting Equation (5.5), we obtain

$$R > \frac{(\mu_d - \mu_c)a}{(\alpha - 1)h^3} \qquad (5.46)$$

So, once we select the suitable parameter α thanks to the graph of Figure 5.7, we'll consequently have a specific lower bound for the resistance of the linking channels in our network. It can be noted that if α increases it is easier to fullfil the previous condition. An increment in this parameter, in fact, corresponds to having more unbalancing between R_n and $R_{eq,n}$ (see Equation (5.5)), thus leading to use longer header droplets in order to deviate the payload in the right branch. In this way, it is more likely that we need header droplets longer than w.

5.3 Bus network performance

In the previous section we focused our attention on studying the concepts and requirements useful to opportunely size a microfluidic bus network such as the one in Figure 5.1. However, a key aspect is still missing before we can move to illustrate of the system performance. The latters, in fact, are strongly affected by a parameter that we haven't considered yet: the input velocity u of the liquid flows in the network. It is patent that, as u increases we will have a corresponding higher "throughput" and vice versa.

Accordingly, we need to find the physical constraints that rule the maximum input velocity (u) sustainable by our network, or, equivalently, the maximum flow rate (Q) since $Q = u*w*h$ where w is the width of the channel and h is its height. Of course, this quantity is influenced by both the necessity of having laminar flow and, thus, low Reynolds number (see Section §2.3) in a microfluidic system and preventing flow degeneration in droplet production (see Section §3.3.2). However, for the typical flow velocities of microfluidic devices (up to tens of mm/s), these requirements are largely satisfied.

Actually, there is another aspect which limits u the most, i.e. the requirement of maintaining the integrity of the drops in correspondence of the bifurcations (see Section §4.1).[5] Let's, in fact, consider Equation (4.1) which discriminates between breakup and non-breakup regime in a T-junction. Specifically, in order to avoid the split of the droplet, we need to satisfy the condition:

$$\frac{L_d}{w} < \chi Ca^{-0.21} \tag{5.47}$$

Now, it is appropriate to express Ca as $\frac{\mu_c u}{\sigma}$ (see Section §2.2). In this way, in fact, it is evident its dependance on u. So, substituting it in Equation (5.47), we get:

$$\frac{L_d}{w} < \chi \left(\frac{\mu_c u}{\sigma}\right)^{-0.21} \tag{5.48}$$

and, inverting the previous formula, we finally obtain:

$$u < \frac{\sigma}{\mu_c} \left(\frac{\chi w}{L_d}\right)^{\frac{1}{0.21}} \tag{5.49}$$

This result tells us that, in general, the maximum input velocity u is limited by both the physical properties of the dispersed and continuous phase (σ, μ_c, χ which depends on the ratio $\frac{\mu_d}{\mu_c}$ and L_d) and the geometry of the system (w). However, realistically, the only parameters that may vary in the network are σ, χ and L_d. The former two depends on the substance that constitutes the dispersed phase but, so as not to weigh down the notation, hereafter we'll consider them constant and equal for both the header and the payload droplets.[6] Conversely, L_d (the length of the droplets) is intrinsically a highly changeable parameter.

---

[5]It is important to notice that, at the first bifurcation of Figure 5.1, $u_c = u_d = u$ which is the velocity setted by the droplet generator. Furthermore, $u_c \leq u$ throughout the entire network, as a consequence of Kirchhoff's current law.

[6]The generalization of this case is, anyway, elementary.

Following this reasoning, in Figure 5.8 we reported the typical trend of the maximum velocity (u) allowed by the system as a function of the droplets length (L_d) in order to avoid their breakup at the bifurcations. The other reference parameters considered here are: $\mu_c = 1.002 \, mPa{\cdot}s$, $\mu_d = 145.5 \, mPa{\cdot}s$, $\chi = 0.187$, $w = 150 \, \mu m$ and $\sigma = 46 \, mN/m$.
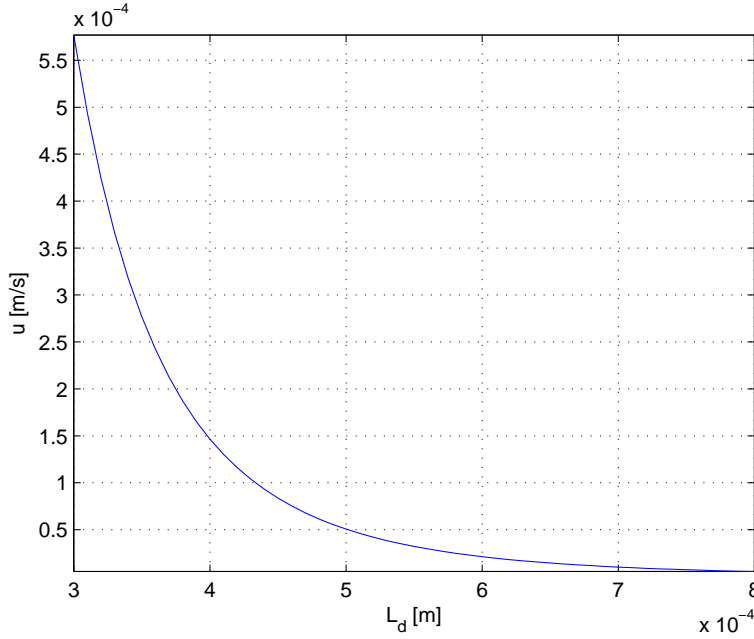

Figure 5.8: Maximum input velocity u allowed for the system as a function of the droplet's length L_d.

Analyzing the graph in Figure 5.8, we notice that u decreases drastically as soon as L_d increases a bit. The latter parameter will, thus, impact strongly on the throughput of the network.

On this purpose, we have seen in Section §5.2 that the header droplet's length varies depending on the number of microfluidic machines (N) in the network and the destination of the payload drop in accordance with Equation (5.11). Specifically, we have realized that we need longer header droplets as N increases. Therefore, the system performance will expire quickly once we add microfluidic machines to the network.

The payload droplet's length, in turn, is defined by the volume of liquid that we want to convey to the microfluidic machine. Now, referring to Equation (5.49), it follows that the longest droplet injected in the system controls the maximum

inlet velocity u allowed. So, as long as the payload droplet is shorter than the header droplet (L_H) the maximum u is fixed by the condition:

$$u < \frac{\sigma}{\mu_c} \left(\frac{\chi w}{L_H} \right)^{\frac{1}{0.21}} \tag{5.50}$$

while, if the length of the payload droplet L_P exceeds L_H, we get:[7]

$$u < \frac{\sigma}{\mu_c} \left(\frac{\chi w}{L_P} \right)^{\frac{1}{0.21}} \tag{5.51}$$

5.3.1 Numerical results

At the end of this dissertation, we are finally able to completely configure the generical microfluidic bus network of Figure 5.1 by setting all its appropriate geometrical and physical parameters. Consequently, we can extract the time required to forward any payload droplet to the target microfluidic machines and, thus, evaluate the "throughput" of the network which is the main aim of the present Section. However, we must first choose a sensible way to define the concept of throughput in a microfluidic system. Reasoning by analogy with the world of telecommunications, the "packets" we want to deliver in a microfluidic network are represented by the droplets. Furthermore, remembering that packets in telecommunication networks are usually weighed according to the amount of information they transport (number of bits), we'll reasonably have to weigh the droplets in microfluidic networks by the amount of substance they carry (volume of liquid). Hence, hereafter, we'll express the throughput in the microfluidic context as the volume of fluid delivered to the output nodes (microfluidic machines) per unit time denoting it with the symbol $R \ [m^3/s]$.

Another dutiful premise, before illustrating the results, concerns the protocol we used to commit resources in our system, i.e. the scheduling policy used to inject droplets in the network. In this regard, we chose the crudest but, at the same time, simplest possible solution which, in practice, consists in sending a couple of header/payload droplets at a time and wait until they have completely left the system before injecting the next one. This rule (a sort of "Stop & Wait" protocol) ensures that the droplets will follow the theoretical dynamics previously exposed. The presence of additional droplets in the systems may, in fact, affect

---

[7]This is true only if we use the same substances for header and payload droplets.

negatively the behavior of the other bubbles, leading to unexpected results. In this regard, we remember that a droplet arriving at a junction, if it does not break, usually goes to the outlet characterized by the highest flow rate. Since droplets can increase hydrodynamic resistance of a channel, the presence of additional droplets downstream in each outlet arm can affect the respective flow rates and, therefore, the partitioning at the bifurcation. This collective hydrodynamic feedback modulated by the increased flow resistance introduced by the droplets can alter the probability of partitioning and, thus, governs the traffic in capillary tubes.

Thus, implementing the "Stop & Wait" protocol, in order to calculate the mean throughput of a generic network with N microfluidic machines we proceed in the following way:

- We fix a uniform length for the payload droplets and size the network basing on the theoretical background seen in the previous sections.

- We reckon the times required to reach each microfluidic machine of the network applying the "Stop & Wait" protocol already described. This could be done by simulating, one at a time, the flow of each pair header/payload.[8] In particular, we obtain, with the aid of Matlab, the so called busy period b_i, $\forall i = 1, ..., N$ which is the time during which at least one the two droplets (header and payload) occupies the system. Clearly, it also coincides with the time we have to wait before injective the successive bubbles due to the "Stop & Wait" mechanism.

- We average these results out of all the destinations, obtaining the mean busy time to reach a microfluidic machines in the referring network: $B = \sum_{i=1}^{N} b_i p_i$, where p_i is the probability of having a payload droplet destined to the i-th microfluidic machine. Hereafter we'll assume a discrete uniform distribution whereby $p_i = \frac{1}{N}$, $\forall i = 1, ..., N$.

- We make the ratio between the volume of the payload droplets and the mean busy period obtaining the desired mean throughput of the network: $R = \frac{Vol}{B}$.

---

[8]We remember that we need different header droplets in order to deviate the payload droplet to different microfluidic machines.

In Figure 5.9 we collect the results obtained for systems with 2, 3, 4 and 5 microfluidic machines considering, from time to time, payload droplets with length equal to L_{d_N}, i.e. the length of the corresponding biggest header droplet of the network. This entails that the maximum input velocity (u) associated to the network is always limited by the payload length (in fact, $L_P \geq L_{d_n}$ $\forall n = 1, ..., N$) in accordance with Equation (5.51).

The general performance ahieved are quite low. This is because we used wide margins to comply the conditions expressed by Equations (5.29) and (5.40), at the expense of throughput. Moreover, the dispersed phase chosen had a very high dynamic viscosity compared to the continuous phase. This implies that we inject in the network a fluid very reluctant to motion (see Section §2.1) which increases considerably the resistance of the channel it occupies and thus decreases the corresponding flow rate. Furthermore, as we already stated, since $\mu_d \gg \mu_c$, the parameter χ in Equation (5.49) is accordingly quite low. This acts, again, as a detriment to performance by limiting significantly the input velocity u of the system.
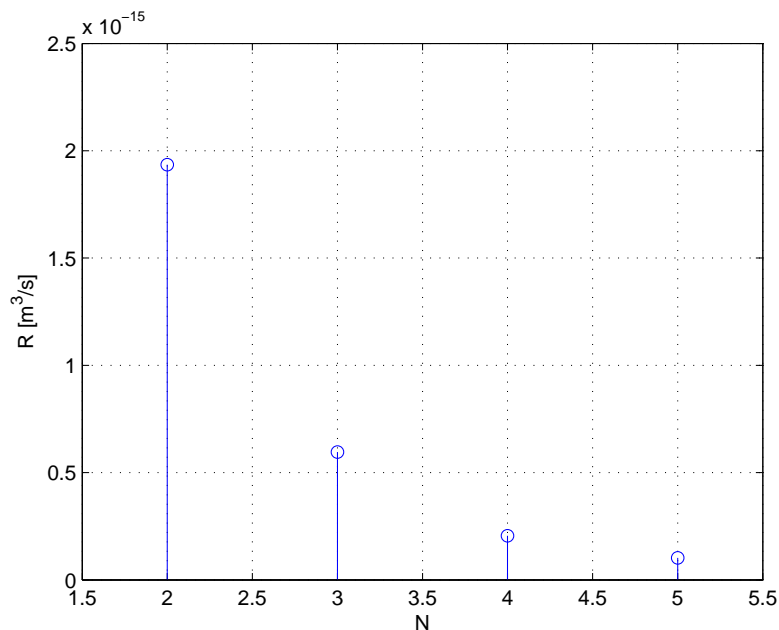

Figure 5.9: Mean throughput of the microfluidic bus network as a function of N for a single payload droplet.

As we expected, the "capacity" of the network expires quickly as N increases.

This is due to three main reasons:

- If we augment N we'll necessarily have greater networks and, thus, the droplets will have to face longer paths before leaving the system.

- In turn, the "Stop & Wait" model adopted to manage the entry of droplets in the systems, strongly penalizes networks with many microfluidic machines. In fact, as we already discussed, it doesn't provide for the simultaneous sending of multiple payload droplets. In this way, we'll have to wait longer before injecting the next payload droplet, as N increases.

- Finally, we have already argued that, once we add microfluidic machines in the system, we'll need corresponding longer header droplets according to Equation (5.11). This will limit the maximum input velocity of the system (see Equation (5.49)) affecting, once again, negatively the throughput of the network.

To conclude our analysis, in Figure 5.10 has been reported the graph, analogous to that of Figure 5.9, obtained by splitting the payload droplet previously considered in two sub-droplets with halved length. In practice, compared to the former case, we have transmitted the same volume of fluid to the microfluidic machines by injecting two bubbles with halved length. The latters, of course, have been sent in two separate sessions because of the "Stop & Wait" model adopted.

The results show a fairly good improvement in the throughput (see Figure 5.11). This could seem counterintuitive since, by halving the payload droplet, we need to forward the resulting pair of sub-droplets in two separate tranche due to the "Stop & Wait" protocol while, in the previous case, a single transmission was sufficient to convey the same volume of fluid to the desired microfluidic machine. However, the reduced dimension of the payload droplets allows us to increase the input velocity of the system in accordance with Equation (5.49). Moreover, as we have already seen, by decreasing the length of the droplets we will also introduce "less resistance" in the channels they occupy and, consequently, the bubbles will move faster. In the case just described, the union of these two factors prevails over the burden of sending droplets in two rounds and, thus, is explained the throughput gain observed.

Therefore, if we have a very long payload droplet, this result tells us that it is convenient to split it in numerous sub-droplets and send them one at a time along
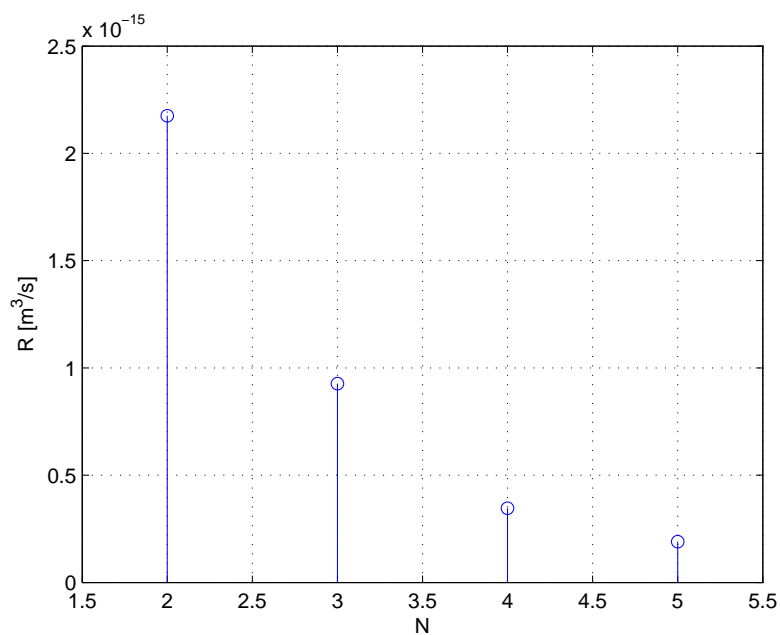
Figure 5.10: Mean throughput of the microfluidic bus network as a function of N for two halved payload droplets.
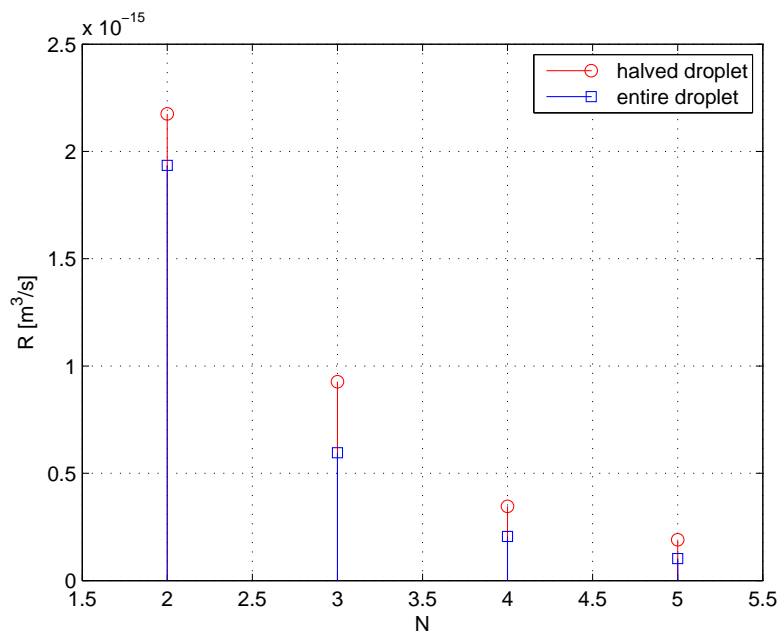

Figure 5.11: Comparison of the mean throughput obtained forwarding a single payload droplet or two halved drops.

our network. Obviously, this rule applies up to a certain point. Indeed, if the granularity of the sub-droplets exceeds a certain threshold, the positive factors seen previously disappear and the splitting acts negatively on the throughput due to the increased number of transmissions required. This critical value is equivalent to the length of the header droplet forwarded with the payload itself. In fact, if we further divide the cargo droplet over this limit, we can't consequently increase the input velocity of the system since, in this case, it is anyhow limited by the header.

In the next chapter we'll give additional tips in order to improve the performance analyzed and we'll introduce alternative networking solutions.

Chapter 6

Future developments

The topic covered in this thesis lends itself easily to improvements and future developments. Among them, a couple of interesting proposals will be briefly discussed in this conclusive chapter.

6.1 Scheduling

In order to enhance the performance of the bus network previously described, it might be thought to a more sophisticated scheduling algorithm, compared to the "Stop & Wait" one, able to manage opportunely the contemporaneous presence of more than one payload droplet in the system. This scenario, unfortunately, entails an exponential increment in the complexity of the system itself. In fact, we've already seen that every drop raises the hydrodynamic resistance of the channel that contains it. Therefore, whenever we inject additional droplets in the network, we vary the volumetric flow rate of the corresponding channel and, cascading, the distribution of the flow rates downstream in each parallel arm. This collective hydrodynamic feedback modulated by the increased flow resistance introduced by the droplets can alter the probability of partitioning and, thus, governs the traffic in capillary tubes leading, in the worst case, to uncontrollable "fluctuations".

However, if kept under control, we could exploit in our behalf such a presence of numerous droplets in the network. Suppose, in fact, that we want to deliver a single droplet to each microfluidic machine connected to the network of Figure 5.1. With the "Stop & Wait" protocol introduced in the previous Chapter we would have to inject a pair of droplets header/payload at a time, wait until they left the

system and then forward the next one.

Conversely, with a more sophisticated scheduler, we could achieve the same goal by injecting toghether all of the payload droplets in the network. This, in fact, would lead to the formation of a train of droplets where the first ones can act as header droplets for the following ones redirecting them to the target microfluidic machines as we saw in Section §4.2. Obviously, this brainwave requires a more thorough analysis of the network and works only if we synchronize opportunely the forwarding of the droplets.

On the other hand, the benefits compared to the "Stop & Wait" algorithm are numerous:

- we can save in terms of physical resources because we don't need anymore to employ a dedicated header droplet for each payload droplet but rather use the payload itself to deviate the following drops;

- we can gain in terms of throughput because we are not forced anymore to wait for the payload droplet to reach its destination before forwarding a new one;

- we are able to commit more effectively the network resources. In this new scenario, in fact, we can convey simultaneously the droplets to the microfluidic machines which can, thus, work in parallel.

6.2 Network topology

Lastly, another interesting flexibility aspect which characterizes a microfluidic network concerns its topology. The bus geometry introduced in this work, in fact, is only one of the configuration that the system may assume. Indeed, at such scale, it is possible to reassemble the network in many different ways depending on our purpose. For instance, a tree-shaped geometry (see Figure 6.1) could be suitably implemented in order to arrange hierarchically the microfluidic machines in the system.

At the end of this thesis it is evident how microfluidics offers great - perhaps even revolutionary - new capabilities for the future. However, a great deal of work remains to be done before it can be claimed to be more than an active
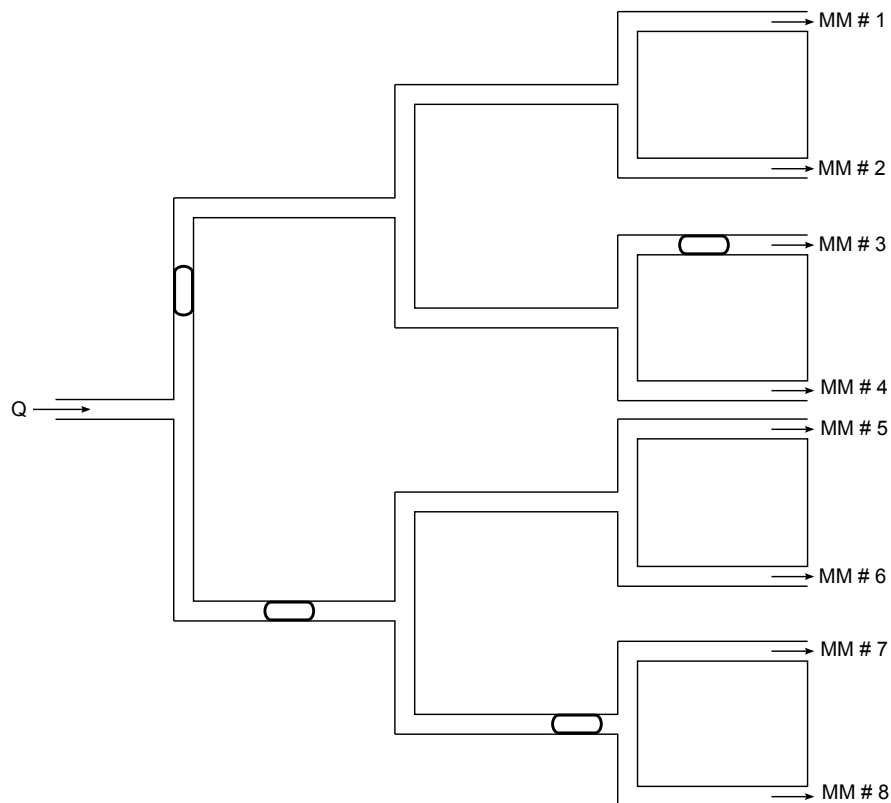
Figure 6.1: Design of a microfluidic tree network.

field of academic research. Nonethless, the fundamentals of the field are very strong: much of the world's technology requires the manipulation of fluids, and extending those manipulations to small volumes, with precise dynamic control over concentrations, while discovering and expoliting new phenomena occurring in fluids at the microscale level must, ultimately, be very important.

Appendix A

OpenFOAM

OpenFOAM (Open Source Field Operation and Manipulation) is a free, open source software package developed by *OpenCFD Ltd* at *ESI Group* and distributed by the *OpenFOAM Foundation*. Basically it works as a *C++* toolbox for the creation of customized numerical solvers, and pre-/post-processing utilities for the solution of continuum mechanics problems, including computational fluid dynamics (CFD).

In the present thesis, we presented a microfluidic study using OpenFOAM to simulate many of the processes described. In particular, the solver to which we have referred is called *interFoam*.

We have used the Volume of Fluid (VoF) method to model the flow of two immiscible fluid (dispersed and continuous phase). In VoF a single set of Navier-Stokes equations for both phases is combined with an advection equation for the fluid fraction α of one of the fluids. In the present work, it is important to underline that both phases are assumed incompressible and Newtonian and the flow is assumed laminar. Hence the general governing equations can be written as:

$$
\begin{cases}
\nabla U = 0 \\
\frac{\partial \rho U}{\partial t} + \nabla \cdot (\rho U U) = -\nabla p + \nabla \cdot \mu (\nabla U + \nabla U^T) + \rho F + F_S \\
\frac{\partial \alpha}{\partial t} + \nabla \cdot (\alpha U) - \nabla \cdot (\alpha (1 - \alpha) U_r) = 0
\end{cases}
\tag{A.1}
$$

where U is the fluid velocity, p is the pressure, ρ the density, μ the viscosity, F a body force and α the volume fraction, which is one in the the bulk of fluid 1 (dispersed phase), zero in the bulk of fluid 2 (continuous phase), and has an

intermediate value in near the interface between the two fluids. F_S, instead, is the surface tension force, modeled as a volumetric force active in the vicinity of the interface only, as described below. The bulk density ρ and viscosity μ in the above Equation (A.1) are computed as weighted averages of two phase properties, based on the fluid fraction α.

The fluid interface is sharpened by introducing the artificial compression term $\nabla \cdot (\alpha(1-\alpha)U_r)$ in the last formula of Equation (A.1), in which U_r describes the artificial compression velocity. This term acts to counteract interface diffusion and is active only on the fluid interface.

The interfacial tension force is approximated as a body force active in interfacial grid cells only, and is formulated as $F_S = \sigma\kappa(\nabla\alpha)$ where σ is the interfacial tension coefficient and $\kappa = \nabla \cdot (\nabla\alpha/|\nabla\alpha|)$ is the curvature of the interface.

The PIMPLE scheme is applied for pressure-velocity coupling. We used a first order Euler scheme for the transient terms, controlling the time step by setting the Courant maximum number to 0.9. Courant number reflects the portion of a cell that a solute will traverse by advection in one time step and is defined as:

$$Co = \frac{u\Delta t}{\Delta l} \tag{A.2}$$

where Δl is the dimension of the grid cell at each location, u is the average linear velocity at that location and Δt is the maximum time step size. When advection dominates dispersion, designing a model with $Co < 1$ will decrease oscillations, improve accuracy and decrease numerical dispersion. Therefore, we are interested in satisfying this condition. A first Gauss linear scheme was used for the discretization of the gradient terms.

The geometry of the three-dimensional channel used has fixed common parameters. In particular, we imposed an uniform width and height for every channel equal to $w = 150\mu m$ and $h = 50\mu m$ respectively. The computational domains and meshes were generated with *blockMesh*, an internal mesh generator of Open-FOAM while the graphical results were viewed using *ParaView* (an open source mutiple-platform application for interactive, scientific visualization).

Bibliography

[1] W. O. Kwang, L. Kangsun, A. Byungwook and E. P. Furlani, "Design of pressure-driven microfluidic networks using electric circuit analogy", *Lab Chip*, **12**, 515-545, 2012.

[2] C. N. Baroud, F. Gallaire and R. Dangla, "Dynamics of microfluidic droplets", *Lab Chip*, **10**, 2032-2045, 2010.

[3] C. Cramer, P. Fischer and E. J. Windhab, "Drop formation in a co-flowing ambient fluid", *Chem. Eng. Sci.*, **59**, 3045-3058, 2004.

[4] D. Funfschilling, H. Debas, H. Z. Li and T. G. Mason, "Flow-field dynamics during droplet formation by dripping in hydrodynamic-focusing microfluidics", *Phys. Rev. E.*, **80**, 15301, 2009.

[5] W. Lee, L. M. Walker and S. L. Anna, "Role of geometry and fluid properties in droplet and thread formation processes in planar flow focusing", *Phys. Fluids*, **21**, 032103, 2009.

[6] H. A. Stone, "On lubrication flows in geometries with zero local curvature", *Chem. Eng. Sci.*, **60**, 4838-4845, 2005.

[7] T. Thorsen, R.W. Roberts, F. H. Arnold and S. R. Quake, "Dynamic pattern formation in a vesicle-generating microfluidic device", *Phys. Rev. Lett.*, **86**, 4163-4166, 2001.

[8] P. Garstecki, M. J. Fuerstman, H. A. Stone and G. M. Whitesides, "Formation of droplets and bubbles in a microfluidic T-junction - scaling and mechanism of break-up", *Lab Chip*, **6**, 437-446, 2006.

[9] M. de Menech, P. Garstecki, F. Jousse and H. A. Stone, "Transition from squeezing to dripping in a microfluidic T-shaped junction", *J. Fluid Mech.*, **595**, 141-161, 2008.

[10] M. J. Fuerstman, A. Lai, M. E. Thurlow, S. S. Shevkoplyas, H. A. Stone and G. M. Whitesides, "The pressure drop along rectangular microchannels containing bubbles", *Lab Chip*, **7**, 1479-1489, 2007.

[11] M.C. Jullien, M. J. Tsang Mui Ching, C. Cohen, L. Menetrier and P. Tabeling, "Droplet breakup in microfluidic T-junctions at small capillary numbers", *Phys. Fluids*, **21**, 072001, 2009.

[12] A. Carlson, M. Do-Quang and G. Amberg, "Droplet dynamics in a bifurcating channel", *Int. J. Multiphase Flow*, **36**, 397-405, 2010.

[13] D. R. Link, S. L. Anna, D. A. Weitz and H. A. Stone, "Geometrically mediated breakup of drops in microfluidic devices", *Phys. Rev. Lett.*, **92**, 054503, 2004.

[14] A. M. Leshansky and L. M. Pismen, "Breakup of drops in a microfluidic T junction", *Phys. Fluids*, **21**, 023303, 2009.

[15] S. Afkhami, A. M. Leshansky and Y. Renardy, "Numerical investigation of elongated drops in a microfluidic T-junction", *Phys. Fluids*, **23**, 022002, 2011.

[16] E. De Leo, L. Galluccio, A. Lombardo and G. Morabito, "On the feasibility of using microfluidic technologies for communications in Labs-on-a-Chip". To appear in Proc. of IEEE ICC 2012.

[17] D. A. Sessoms, M. Belloul, W. Engl, M. Roche, L. Courbin and P. Panizza, "Droplet motion in microfluidic networks: Hydrodynamic interactions and pressure-drop measurements", *Phys. Rev. E.*, **80**, 016317, 2009.

Ringraziamenti

Ci tengo innanzitutto a ringraziare i miei genitori, a cui dedico questa tesi, visto che senza il loro costante supporto e appoggio non sarei mai riuscito a raggiungere questo importante traguardo. Grazie, in particolare, per avermi sempre sostenuto nelle mie scelte di vita, facili e difficili, senza mai farmele pesare e per i saggi consigli e l'enorme affetto che non mi avete mai fatto mancare. Ringrazio inoltre mia sorella, a cui tengo molto anche se non sempre lo dimostro a dovere, per essere sempre presente quando ho bisogno di lei e per le parole di conforto che sa dispensare nei momenti bui. Grazie anche a mio cugino Giovanni, con cui sono cresciuto assieme, per il suo carattere che lo rende unico ed insostituibile e a mia cugina Marina per le fenomenali ospitate a Bologna (ovviamente, per questo, ringrazio anche a Massimo).

Un doveroso ringraziamento va poi al prof. Andrea Zanella, che reputo una delle persone più competenti ed appassionate nello svolgimento del proprio lavoro. Lo ringrazio per gli utili suggerimenti e per le "lavagnate" di conti riempite assieme senza i quali non sarei certo riuscito a portare a termine questa tesi.

Ringrazio Maria che, da quando ho ricordi, ha contribuito con grande affetto a crescermi e a farmi diventare la persona che sono ora.

Ringrazio Francesco P. (Spazzola), Francesco L. (Sonda) e Chethan per la forte e sincera amicizia che ci lega, per i pomeriggi di svago trascorsi assieme e per le lunghe chiacchierate che hanno il notevole pregio di farmi dimenticare i miei problemi. Grazie anche all' inseparabile ed insostituibile compagnia del mare che, anche se la vedo solo per un mese all'anno, riesce sempre a rendere indimenticabili le mie estati.

Ringrazio inoltre i miei compagni di Università, sia della triennale (soprattutto Calle, Michi, Pelle, Davide e Valentina) che della magistrale (in particolare Claudio, Silvia, Leo e Alex), per essere riusciti a rendere molto meno pesanti i faticosi anni di studio di Ingegneria, e tutti gli "apprendisti Telecom" per rendere il lavoro un'esperienza piacevole.

Infine, rivolgo un sincero ringraziamento alla persona con cui ho trascorso tutta la vita e che più di tutte mi capisce (d'altronde c'è "telepatia"), ovvero...a mio gemello Alessandro.

Insomma, se ancora non si era capito, a tutti voi e a tutte le altre persone che mi hanno sopportato e supportato volevo semplicemente dire: "grazie di esistere".